3D Radiative Transfer Simulation of Starspots in Stellar Atmospheres

Diploma Thesis
by
Alexander Berkner

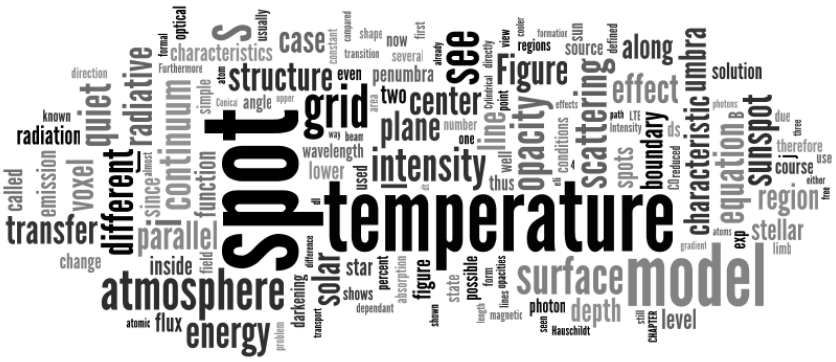

Hamburger Sternwarte
Fachbereich Physik
Universität Hamburg

September 27, 2011

Erstgutachter: Prof. Dr. Peter Hauschildt
Zweitgutachter: Prof. Dr. Robi Banerjee

hamburger sternwarte

Abstract

Sunspots are regions where the solar magnetic field inhibits the convection process in the photosphere, resulting in cooler zones, which are perceived as darker spots on the solar surface. This work describes the simulation of sunspots and starspots with the multi purpose stellar atmosphere code PHOENIX. We have modified a mostly plane parallel 3D atmosphere structure with several different models for sunspots. These models range from simple cylindrical regions of constant temperature to more complex models with continuous temperature gradient between spot center and quiet atmosphere. The radiation transfer problem was solved in three dimensions for these configurations.

Our goal was to study, in what way three dimensional temperature features like sunspots affect the radiative transport within a stellar atmosphere and what effects on the total spectrum of a star can be expected. Since a sunspot or starspot, as a cooler region of the stellar atmosphere, affects molecular lines more strongly, we have focused on several carbon monoxide bands as an example.

The models were tested with an NLTE two level atom solver. Here, the temperature was modified without consideration of the resulting change to the chemical composition of the atmosphere. As as second step, the simulation was expanded to include a solution of the LTE equation of state for each voxel. With this, it was possible to determine, in which regions of the spot model the CO concentration was affected the most, and, furthermore, what these effects meant for the resulting spectra. As we expected, CO lines are affected more strongly than atomic lines originating from deeper, hotter layers of the atmosphere.

The results for the chemical composition where transferred back to the two level atom solver, which is capable of including line scattering with complete redistribution into the calculation. Here, we found that scattering strongly influences the profile of the visible part of the spot.

Finally, we investigated how three dimensional structures appear from different angles of view. We compared center to limb variation for the spot umbra with the normal center to limb variation of simple plane parallel structures. The presence of the sunspot with its non plane parallel opacity structure results in a more complex difference between direct view and view from high angles. The umbra is actually brighter, compared to its surroundings, when seen at high angles. Here, the shape of the spot model has a strong influence on the result.

Zusammenfassung

Sonnenflecken sind Zonen, in denen die Konvektion innerhalb der Photosphäre durch das solare Magnetfeld behindert wird. Die sich daraus ergebende Abkühlung ist als dunklerer Bereich auf der Oberfläche der Sonne wahrzunehmen. Diese Arbeit beschreibt die Simulation von Sonnen- und Sternflecken mit Hilfe des Sternatmosphären-Codes PHOENIX. Grundlage der Berechnungen bildete eine hauptsächlich planparallele Schichtung, deren Temperaturstruktur innerhalb eines gewissen Bereichs durch verschiedene Modelle modifziert wurde. Hierbei reichten die verwendeten Modelle von einfachen Zylindern von konstanter Temperatur bis zu komplexeren Formen, in welchen ein kontinuierlicher Übergang zwischen der reduzierten Temperatur des Umbrae und dem ungestörten Außenraum berücksichtigt wurde.
Ziel war es, zu untersuchen in welcher Art und Weise dreidimensionale Strukturen wie Sonnenflecken sich auf den Strahlungstransport innerhalb einer stellaren Atmosphäre auswirken. Es wurden sowohl oberflächenaufgelöste Spektren, als auch integrierte Spektren der gesamten Oberfläche berechnet. Aufgrund der reduzierten Temperatur von Stern- und Sonnenflecken ist mit einer vermehrten Bildung von Molekülen zu rechnen, die sich nur bei diesen Temperaturen bilden können. Aus diesem Grund wurden in erster Linie Kohlenstoffmonoxid (CO) Linien- und Bandspektren untersucht.
Zunächst wurde der Strahlungstransport mit Hilfe einer NLTE Simulation eines Zwei-Level-Atoms für eine einzige Linie berechnet, um die Auswirkungen einer reinen Temperaturänderung ohne Berücksichtigung der veränderten Atmosphärenchemie zu bestimmen. Anschließend wurde in einem zweiten Schritt auch die Zustandsgleichung im lokalen thermischen Gleichgewicht abhängig von den veränderten Temperaturen gelöst. Hierdurch konnte bestimmt werden, in welchen Bereichen des Flecken-Modells besonders viel zusätzliches CO zu erwarten ist. Als Grundlage diente hierbei das Modell eines normalen G-Typ Sterns.
Wie erwartet ist die Wirkung auf temperatursensible Spektrallinien wie CO deutlich ausgeprägter als die Wirkung auf atomare Linien, welche in tieferen Schichten, bei höheren Temperaturen entstehen. Mit der gleichen chemischen Zusammensetzung wurde die Rechnung anschließend im NLTE Zwei-Level-Atom wiederholt. Hierbei zeigte sich, dass Streuung einen starken Einfluss auf das Profil des an der Oberfläche sichtbaren Flecks hat.
Abschließend wurde untersucht, in welcher Art und Weise dreidimensionale Strukturen in der Atmosphäre unter unterschiedlichen Sichtwinkeln erscheinen, insbesondere im Vergleich zur normalen Mitte-Rand-Verdunklung der planparallellen Vergleichsstruktur. Hierbei zeigte sich, dass das Sonnenfleckenmodell am Rand deutlich heller erscheint als im Zentrum des Sichtfelds, wobei das genaue Verhalten von der Größe des Modells abhängig ist.

Contents

Chapter 1

Introduction

It has been known for a long time that the surface of the sun is not perfectly uniform. It is frequently covered by darker spots, at rare times even large enough to be observed with the naked eye. These so called *sunspots* have been observed for well over two thousand years from all over the world. The oldest known references to sunspots date back to ancient China during the times of the Han Dynasty in 28 B.C. However, it was still a long time before a conclusive interpretation of the phenomenon was found. As far as we know today, sunspots were, if explained at all, mostly mistaken to be transiting inner planets.

The first one to correctly identify sunspots as being part of the solar surface, was the Italian astronomer and natural philosopher Galileo Galilei at the beginning of the seventeenth century in *Istoria e Dimostrazioni intorno alle Macchie Solari*, which was published in 1613. [Galilei, 1613] One of the effects that was confirmed by use of this assumption was the rotation of the sun. In this way, sunspots have proven to be an instrument in observing other properties of the sun for almost four hundred years.

In modern times, the nature of sunspots as cooler regions of the stellar photosphere has long since been accepted. Sunspots are observed and measured by high resolution imaging of the solar surface as well as techniques like *helioseismology*, which allows to probe into deeper layers beneath the solar surface, thus, giving us information about the depth structure of sunspots.

Yet, while we have a multitude of methods to observe spots on the surface of our own sun, observing spots on other stars is still extremely difficult. We can assume that many, if not all, stars show spots of some sorts, since it is unlikely that this is a unique feature of our own sun. Nevertheless, it is impossible to resolve the surface of distant stars directly. Of course, it is possible, and has first been suggested and applied by Kron [1947], to measure measure changes in a stars light curve and thus detect spot coverage by variations due to the stars rotation and the effect that the spot forms and decays within a time-frame of days or month. However, today a similar method of detection is used for the identification of *extrasolar planets* and even while those do not tend to vanish after any observable amount of time, the possibility of false detection exists both ways.

Nevertheless, extrasolar planets prove to be not only a possibility for false detection, but a chance for observation of starspots, since they allow a limited possibility to reconstruct parts of a stars surface from a planets transit lightcurve. The interested reader is here referred to Huber [2010].

Since a spot represents not only a darker part of the stellar surface but first and

foremost a cooler region of the stellar atmosphere, we can validly assume to see an increased concentration of molecules like water, titan oxide or carbon monoxide inside them, and, therefore, a deepening of molecular lines and band spectra, even in the non-surface-resolved spectra we observe for distant stars. In this way, starspots have been identified by the so-called line-depth ratio method, where different spectral lines are compared to obtain information about the temperature variations across a stars surface. See e.g. Catalano et al. [2002].

Over the last ten years, the available computer power has been vastly increased due to the implementation of multi processor computing on large scales with clusters of several thousand central processing units and several terabytes of total available memory. This means that the simulation of a three dimensional structures in stellar atmospheres is finally possible within a reasonable amount of time and we are no longer limited to stars of spherical symmetric geometry, where structures that require a lateral variation in the stellar atmosphere cannot be included.

In this work, we begin to implement simple models of spot structures into the 3D radiative transfer simulation part of the multi purpose stellar atmosphere code PHOENIX. Comparison between synthetic spectra calculated with PHOENIX/1D have been used for interpretation of spectroscopic data for over a decade. [Hauschildt, 1992, 1993, Hauschildt and Baron, 1999]

By simulating radiative transfer for distinct three dimensional structures like starspots, we expect to improve our synthetic spectra for comparison with observations, and thus better interpretation of stellar spectra. Of course, it is impossible to simulate any of the infinite number of possible configurations of sunspot coverage for a stars surface. Nevertheless, by improving our synthetic spectra, we can, at least, investigate, what we can expect to observe in the spectra of a starspot covered star.

From observations of the sun, we know that there is some CO present in the upper regions of the solar atmosphere, which can be observed close to the limb of the solar disk. The formation of CO in the solar atmosphere has been investigated e.g. by Uitenbroek [2000a,b]. In this work, we have focused on the effects that a simple model of a starspot would have on the formation of CO in a stellar atmosphere and, therefore, what changes to different lines in a CO band we can expect to observe.

Chapter 2

Theory of Stellar Atmospheres

Stellar atmospheres cannot be described without considering both matter inside the atmosphere and radiation passing through the atmosphere, as well as the interaction between them.

The atmosphere itself consists of layers of atoms and molecules gravitationally bound to the mass of the star and shaped by a balance of inward gravitation and outward gas pressure. Energy produced by nuclear fusion inside the stellar core is distributed into the atmosphere by both radiative and convective processes. Any radiation originating from the inside of the star is bound to interact with atmospheric matter while traversing the atmosphere. Therefore, the outgoing radiation is influenced by the atmosphere's physical conditions such as temperature, density, chemical composition and atomic state of excitation. Likewise, as an important source of energy, the traversing radiation has a strong feedback onto these physical conditions.

Thus, the state of the atmosphere has a strong influence on any light that leaves the star and, therefore, on every observation of the star.

This chapter summarizes the central mechanism of interaction between radiation and matter, the principles of radiative transfer and several effects that are direct consequences of this process such as *Limb Darkening*, which is important for this work. Where not specified otherwise, the descriptions in this chapter are based upon the works of Rutten [2003], Mihalas [1970, 1978] and references therein. For a more detailed description of how the problem of radiative transfer is solved numerically see chapter 3.

2.1 Radiative Transfer

Any volume element of matter dV crossed by a beam of light can add energy to and remove energy from the beam. The net intensity I_ν at a specific frequency ν of the traversing beam is, thus, either increased or reduced during the passage. Processes that increase the intensity are called emissive, while, on the other hand, processes that reduce intensity are called extinctive.

For the emission along a path ds we can define the emissivity j_ν for a frequency ν as the local intensity contribution to the beam per unit length:

$$dI_\nu = j_\nu(s) \cdot ds \tag{2.1}$$

Likewise we can define the opacity by writing

$$dI_\nu = -\chi_\nu(s) \cdot \rho \cdot I_\nu(s) \cdot ds \tag{2.2}$$

for purely extinctive media. The absolute extinction from the beam is, hence, proportional to the intensity I_ν of the beam itself. The opacity is given per unit mass and length, so that ρ is the mass density along the path.

The standard form of the radiative transfer equation can be derived by summation over extinction from the beam and emission into the beam, which net to a total of

$$dI_\nu(s) = j_\nu \cdot ds - \rho\chi_\nu I_\nu \cdot ds$$

Therefore the change of intensity dI_ν along a line element ds is

$$\frac{dI_\nu}{ds} = j_\nu - \chi_\nu \rho I_\nu \tag{2.3}$$

or, by defining the source function S_ν as

$$S_\nu = \frac{j_\nu}{\chi_\nu} \tag{2.4}$$

can be written as

$$\frac{dI_\nu}{\chi_\nu \rho \cdot ds} = S_\nu - I_\nu \tag{2.5}$$

For the purpose of describing radiative transfer in stellar atmospheres it is far more convenient to use an optical path length defined by the extinction, called the *optical depth* τ, where $d\tau$ is differentially defined via

$$d\tau_\nu = -\rho\chi_\nu ds \tag{2.6}$$

This leads to the radiative transfer equation along the path of a photon ds, which is usually called a characteristic.

Under the assumption of a plane parallel or a spherically symmetric atmosphere, it is possible to use τ as a depth scale parallel to $\vec{e}_z$ or $\vec{e}_r$. The different possible characteristics through the plane parallel structure can then be distinguished by use of the angle ϑ from the z direction with

$$dz = \cos(\vartheta) \cdot ds = \mu \cdot ds$$

Now the radiative transfer equation (2.5) can be rewritten into its standard form for plane parallel atmospheres:

$$\mu \frac{dI_\nu}{d\tau_\nu} = I_\nu - S_\nu \tag{2.7}$$

This equation describes the transport of radiation along a specific characteristic of angle μ to the normal. At this point, it would be possible to calculate a solution for any single angle of view, as long as the source function S_ν is already known, which is usually not the case, as is described below.

In the three dimensional case, the basic equation of radiative transfer is similar, though a characteristic can not only be described by ϑ or $\mu = \cos(\vartheta)$, since both the phase space coordinates of the characteristic, and the spatial coordinates of the boundary point of the characteristic are needed. This is described in more detail in chapter 3.

2.2 Photon-Matter Interactions

There are several different processes that contribute to extinction, or, more pricisely, the interactions between the photons of a radiation field and electrons or atoms. Atoms have a ground state, defined by the electron configuration of lowest energy, and a theoretically infinite number of excited states. In real conditions, the number of excited states is limited by the existence of other atoms in the vicinity. Each configuration of the electron shell corresponds to a distinct energy level, so that any transition between two possible configurations requires either the introduction of additional energy into the system or the removal of energy that was previously bound in the system. The energy that is either required or released is the energetic difference between the two states that are involved in the transition. For a transition $j \to i$ this results in

$$E_{ji} = E_i - E_j \tag{2.8}$$

This permits several possible interactions between atoms and a radiation field. A photon of energy $E_\nu = h\nu$ can be absorbed by an atom in at least two ways:

If $E_\nu \geq E_i$ where E_i is the energy of any currently populated atomic level, the bound electron in said state can be removed into the continuum with the excess energy as kinetic energy and the photon is destroyed. This process is called *photo ionization* or *bound-free absorption*.

$$A + \gamma \longrightarrow A^+ + e^-$$

The second possibility is that the photon energy E_ν matches the energetic window ΔE between two atomic states thus exciting an electron into one of its upper energy levels in a process usually called *photo excitation*.

$$A + \gamma \longrightarrow A^*$$

The atom eventually returns to its ground state. The excess energy is, hereby, released by emission of at least one photon, which is likely to be slightly different both in wavelength and in angle of emission, due to the finite width of the transition.

$$\begin{aligned} A^* &\longrightarrow A + \gamma' \\ &\longrightarrow A + \gamma'' + \gamma''' + ... \end{aligned}$$

This process is known as *line scattering*. The other possibility is that the atom collisionally distributes the excess energy into the thermal pool of the atmosphere without creation of another photon. This is called *collisional de-excitation*.

$$A^* \longrightarrow A + E_{\text{thermal}}$$

Furthermore, photons can be absorbed or scattered not only by atoms, but also by free electrons which may exist among the atoms. Upon absorption, the electron receives the photon energy as additional kinetic energy. This is called the *free-free absorption*. If the photon is not absorbed but redistributed with respect to wavelength or scattered into a different angle, we speak of *Thomson scattering*.

Both different types of scattering and different types of absorption contribute to the total opacity χ_ν as defined by equation 2.2, which can be written as

$$\chi_\nu = \kappa_\nu^c + \kappa_\nu^l + \sigma_\nu \tag{2.9}$$

where κ_ν^c is the so called *continuum absorption coefficient* or *continuum opacity* per gram of stellar matter for bound-free transitions and κ_ν^l is the *line opacity* for bound-bound transitions, while σ_ν is similarly defined for the sum of all scattering processes.

Stimulated Emission

Atoms may not only absorb or scatter photons that are already present in the radiation field. An atom that is in an excited state may return to an energetically preferable state under emission of a photon carrying the excess energy. Furthermore, an excited atom A^* in the upper level of a transition with energy E_{ij} can interact with a photon γ of identical energy $E_\nu = h\nu = E_{ij}$ by dropping back to the lower state A under emission of a new photon γ that has the same wavelength, phase and angle as the original photon. We can write this reaction as

$$A^* + \gamma \longrightarrow A + 2 \cdot \gamma$$

This process is called *stimulated emission*. It is common practice to treat stimulated emission not as additional emission, but instead as negative absorption, because of its dependence on intensity, and, thus, correct the respective absorption coefficients.

Molecular Absorption

Molecules can interact with radiation in exactly the same way as atoms do. However, the number of possible energy levels a molecule possesses is considerably higher. Atoms have only a single atomic nucleus and therefore an atomic configuration that is complex, but has only a relatively small number of degrees of freedom. In the case of molecules the same number of freedoms for the electronic shell are supplemented by the degrees of freedom for the interactions between the nuclei of the atoms forming the molecule. This is an additional multi body problem, which allows for both rotational and vibrational energy levels.

This results in a great number of energetic levels with small energetic differences, corresponding to the same electronic structure, but a different state of rotation or vibration of the different atomic nuclei that are forming the molecule. In this way, the molecular spectrum shows band spectra with a great number of lines within close proximity. These structures are usually called band spectra.

In this work, we have focused on Carbon Monoxide (CO), which is a diatomic molecule, consisting of one carbon ${}_6$C and one oxygen ${}_8$O atom, connected by triple covalent bonds with six shared electrons, and a total of 14 electrons. With two atomic nuclei, there are

two rotational and one vibrational degree of freedom for the nuclei themselves. CO is transparent in the visible part of the spectrum, but has several band spectra in the near and deep infra-red around 23000 Å and 44000 Å.

For more details on molecular physics, see e.g. Haken and Wolf [2006].

2.3 Formal Solution

If the Source function S would be known throughout the atmosphere, it would be possible to solve the problem of radiative transfer by integration due to the fact that equation (2.7) is a linear first order differential equation in $I(\tau_\nu)$. Since $S = S(\tau_\nu)$ itself is depending on the optical depth, and as we will show below the mean intensity $J(\tau)$, one cannot obtain a full solution analytically. Nevertheless, it is possible to write the *formal solution* of equation (2.7) as

$$I_\nu(\tau_\nu, \mu) = I(0, \mu) \cdot e^{-\frac{\tau_\nu}{\mu}} + \int_0^{\tau_\nu} S(t) \cdot e^{\frac{t-\tau_\nu}{\mu}} \cdot \frac{1}{\mu}\, dt \tag{2.10}$$

here written for a case, with $I(0, \mu)$ as boundary conditions.

In *thermodynamic equilibrium* (TE), a state where the temperature T would be uniform throughout a perfectly absorbing medium, the source function is quite simple. The state of excitation of all atoms and molecules inside this kind of medium is then given by the *Boltzmann distribution function*

$$\left[\frac{n_{r,s}}{n_{r,t}}\right]_{\mathrm{TE}} = \frac{g_{r,s}}{g_{r,t}} \cdot \mathrm{e}^{-(E_{r,s}-E_{r,t})/(kT)} \tag{2.11}$$

k is Boltzmann's constant, $n_{r,s}$ is the number density of atoms in level s of ionisation stage r, and $g_{r,s}$ is the statistical weight of level s of stage r. In this case, $(r, s) = (r, 1)$ would be the ground level of ionisation stage r. $(E_{r,s} - E_{r,t}) = E_\nu = h\nu$ is the transition energy between for a radiative transition between levels (r, s) and (r, t).

As as result, we would see the well known Planck function for the blackbody radiation:

$$S_\nu = B_\nu(T) = \frac{2h\nu^3}{c^2} \frac{1}{\exp\left(\frac{h\nu}{kT}\right) - 1} \tag{2.12}$$

Therefore, solving the radiative transfer equation (2.7) is simple for this kind of medium, where we already know the source function for all points. Still, a star is anything but in thermodynamic equilibrium with a uniform temperature. There is a strong difference between a stars surface temperature and the stellar core region where temperatures of several million K are caused by nuclear fusion. Thus, it can be expected that even in the outermost layers of the star, there is a temperature gradient.

Despite, we can often assume that the relevant thermodynamic properties such as atomic occupation numbers, *opacity* χ_ν and *emission* j_ν inside a finite volume element at position $\vec{r}$ of the atmosphere are the same as the TE values for the local Temperature $T = T(\vec{r})$, so that equation (2.12) can be assumed as valid. This assumption is called the *local thermodynamic equilibrium* (LTE) approximation. It requires that the mean free path of photons is short compared to the dimensions of the medium.

Obviously, this approximation is not valid for all cases, so that there needs to be a method to include different effects of *non local thermodynamic equilibrium* (NLTE). In full NLTE the level population is no longer given by equation (2.11), so that we need to solve the rate equations for each level directly, which is extremely time-consuming.

The Influence of Scattering

One such effect that renders a direct solution of the radiative transfer problem impossible is photon scattering. If $\sigma_\nu \neq 0$, the emission of an element of volume dV does not depend solely on the temperature of the medium inside this element, since scattering causes emissions that are proportional to the number of photons available, and, therefore, dependant of the intensity I_ν. In this way, scattering connects different parts of the atmosphere, hence, any assumption that is based solely upon local conditions may not be valid.

The actual dependence of the scattered emission j_ν^s is related to the type of scattering, i.e., the solid angle and frequency redistribution of scattered photons. This dependence can be expressed as a function $R(\nu', n'; \nu, n)$ so that it is possible to write any form of scattering as

$$j_\nu^{\text{scattering}} = \sigma_\nu \oint_{4\pi} \int_0^\infty I'_\nu \cdot R(\nu', n'; \nu, n) \cdot d\nu' \frac{d\Omega}{4\pi} \tag{2.13}$$

Under the assumption of coherent and isotropic scattering, the redistribution function is $R(\nu', n'; \nu, n) = \delta(\nu - \nu')$ and the emission by scattering is proportional to the mean intensity J_ν which is defined as

$$J_\nu = \frac{1}{4\pi} \oint I_\nu d\Omega \tag{2.14}$$

With this, it is possible to derive the source function for a combination of LTE thermal emission with coherent and isotropic scattering. The total emission j_ν then adds up to

$$\begin{aligned} j_\nu &= j_\nu^{\text{thermal}} + j_\nu^{\text{scattering}} \\ &= \kappa_\nu \cdot B_\nu + \sigma_\nu \oint_{4\pi} \int_0^\infty I_{\nu'} \delta(\nu - \nu') d\nu' \frac{d\Omega}{4\pi} \\ &= \kappa_\nu \cdot B_\nu + \sigma_\nu J_\nu \end{aligned} \tag{2.15}$$

The source function S is then derived as

$$\begin{aligned} S_\nu &= \frac{j_\nu}{\chi_\nu} \\ &= \frac{\kappa_\nu}{\kappa_\nu + \sigma_\nu} B_\nu + \frac{\sigma_\nu}{\kappa_\nu + \sigma_\nu} J_\nu \end{aligned}$$

Now a scattering parameter ε_ν can be defined as

$$\varepsilon = \frac{\kappa_\nu}{\kappa_\nu + \sigma_\nu} \tag{2.16}$$

which results in

$$S_\nu = (1 - \varepsilon_\nu) J_\nu + \varepsilon_\nu B_\nu \tag{2.17}$$

This means that in all but the most simple cases of pure LTE, the source function S_ν itself, which is needed to compute the formal solution of the radiative transfer equation (2.7), is dependant of I_ν. This is the reason why it is usually impossible to compute I_ν directly.

2.4 Iterative Solution

In plane parallel geometry the formal solution (2.10) can be written as

$$I_\nu(\tau_\nu, \mu) = \int_{\tau_\nu}^{\infty} S_\nu(t) \cdot \exp\left(-\left(t - \tau_\nu\right)\right) \frac{dt}{\mu} \qquad (0 \leqslant \mu \leqslant 1) \tag{2.18}$$

$$I_\nu(\tau_\nu, \mu) = \int_{0}^{\tau_\nu} S_\nu(t) \cdot \exp\left(-\left(\tau_\nu - t\right)\right) \frac{dt}{-\mu} \qquad (-1 \leqslant \mu \leqslant 0) \tag{2.19}$$

for both outgoing and incoming rays. In this case the boundary conditions are applied so that there is no incoming radiation ($I_\nu\left(\tau_\nu = 0, \mu < 0\right) = 0$) and the boundary for outgoing rays is at $\tau = \infty$. Insertion of this form of the *formal solution* into equation (2.14) yields

$$J_\nu(\tau_\nu) = \frac{1}{2} \int_{-1}^{1} I_\nu(\tau_\nu, \mu) d\mu \tag{2.20}$$

$$= \frac{1}{2} \left[\int_0^1 \int_{\tau_\nu}^{\infty} S_\nu(t) \cdot \exp\left(-\left(t - \tau_\nu\right)\right) \frac{dt}{\mu} d\mu + \int_{-1}^{0} \int_{0}^{\tau_\nu} S_\nu(t) \cdot \exp\left(-\left(\tau_\nu - t\right)\right) \frac{dt}{-\mu} d\mu \right]$$

This equation can be rewritten into a more convenient form by interchanging the order of integration which is possible because μ and τ are independent of each other. Furthermore it is possibly to shorten the expression by introduction of the exponential integral which is defined as

$$E_n(x) = \int_1^{\infty} t^{-n} e^{-xt} dt \qquad n \in \mathbb{N} \tag{2.21}$$

Applied to equation (2.20) this provides the so called Schwarzschild equation for J_ν (for the complete derivation see Mihalas [1978] page 40):

$$J_\nu(\tau_\nu) = \frac{1}{2} \int_0^{\infty} S_\nu(t_\nu) E_1\left|t_\nu - \tau_\nu\right| dt_\nu \tag{2.22}$$

This allows to compute J_ν directly when the Source function is known. This equation is usually written in operator form as:

$$J_\nu = \Lambda\left[S_\nu\right] \tag{2.23}$$

where Λ is an abbreviation for

$$\Lambda\left[f(x)\right] = \int_0^{\infty} f(x) \cdot E_1\left|t_\nu - \tau_\nu\right| dt \tag{2.24}$$

Thus far it is possible to calculate both I_ν and J_ν in the case of an already known source function S_ν as well as to express the source function itself in terms of J_ν and B_ν. What is still needed is a scheme that allows for calculation of S_ν without prior knowledge of J_ν. We start by simply inserting (2.17) into equation (2.23) as follows:

$$J_\nu = \Lambda\left[S_\nu\right] = \Lambda\left[\left(1-\varepsilon_\nu\right)J_\nu + \varepsilon_\nu B_\nu\right] \tag{2.25}$$

The problem is now reduced in such a way that J_ν is only dependent on itself and the form of B_ν, where the latter is known from the temperature structure of the atmosphere. J_ν can now be calculated by use of an iterative scheme using the LTE condition $S_\nu = B_\nu$ as a starting condition and an iteration of the form

$$J_{new} = \Lambda\left[\left(1-\varepsilon_\nu\right)J_{old} + \varepsilon_\nu B_\nu\right] \tag{2.26}$$

This simple scheme is usually named Λ *iteration*. Unfortunately this kind of iterative solution shows an extremely slow convergence behaviour for large optical depth and small values of ε_ν, see e.g. Hauschildt and Baron [2006], so that it is impossible to achieve a solution within a reasonable amount of time.

Operator Splitting

The basic scheme of Λ iteration can be modified to improve convergence behaviour by employing an operator splitting method, see Cannon [1973]. This is done by modifying equation (2.23) and adding a zero by adding and subtracting a new operator Λ^*:

$$J_\nu = \left((\Lambda-\Lambda^*)+\Lambda^*\right)[S_\nu] = \Lambda^*[S_\nu] + (\Lambda-\Lambda^*)[S_\nu] \tag{2.27}$$

From this a new iteration scheme for $J^{(n)} \rightarrow J^{(n+1)}$ can be derived as

$$J_\nu^{(n+1)} = \Lambda^* S_\nu^{(n+1)} + (\Lambda-\Lambda^*)\cdot S_\nu^{(n)} \tag{2.28}$$

using equation (2.17) this leads to

$$\left(1-\Lambda^*(1-\varepsilon_\nu)\right)\left[J_\nu^{(n+1)}\right] = \underbrace{\Lambda\left[S_\nu^{(n)}\right]}_{J_{\mathrm{FS}}} - \Lambda^*(1-\varepsilon_\nu)[S_\nu^{(n)}]$$

where the brace marks the formal solution J_{FS} that results from application of Λ to the old source function $S^{(n)}$. This gives the next iteration step as

$$J_\nu^{(n+1)} = \left(1-\Lambda^*(1-\varepsilon_\nu)\right)^{-1}\left[J_{FS} - \Lambda^*(1-\varepsilon_\nu)[S_\nu^{(n)}]\right] \tag{2.29}$$

To solve this equation, only the approximate lambda operator Λ^* has to be inverted, which reduces the numerical effort of the problem considerably. [Hauschildt and Baron, 2006].

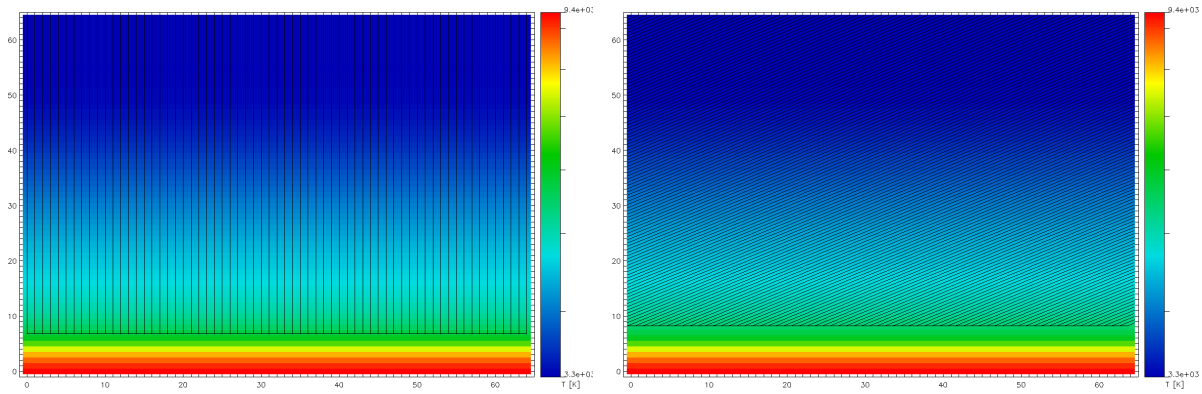

(a) $\vartheta = 0°$ ($\mu = 1$) (b) $\vartheta = 60°$ ($\mu = 0.5$)

Figure 2.1: Characteristics for different ϑ drawn from the surface of the plane parallel grid to the level of $\tau = 1$, which is marked by the black horizontal line. The color shows the temperature of each layer in logarithmic steps between 3300 and 9400 K.

2.5 Limb Darkening

It is known from observations that a star is less bright at its rim, than compared to a direct look at its center - even if the surface of the star is completely spherically symmetric in its structure. This so called *limb darkening*, thus, is not caused by lateral variations of the physical conditions in the stellar atmosphere.

In a plane parallel case, which is at least true for a point of view close to the star and a uniform surface structure, this effect can be derived directly from equation (2.6) with $dz = \mu \cdot ds$ and therefore

$$d\tau_\nu = \chi_\nu \frac{dz}{\mu} \tag{2.30}$$

The direct view into the center of the star is hereby equivalent to $\vartheta = 0$ or $\mu = 1$, while the characteristic to the rim of the star is equivalent to $\vartheta > 0$ and therefore $\mu < 1$. Assuming that all relevant physical variables are dependant on z only, we can see immediately that for any $\mu < 1$ the same optical depth τ_ν is reached at shallower depth z.

The radiation that reaches the surface and can thus be observed is dominated by radiation produced at $\tau_\nu = 1$. In the photosphere the temperature typically rises with depth and the emitted radiation depends on the temperature, we see into shallower and thus darker regions of the atmosphere, if the characteristic we follow increases in angle. (See figures 2.1 and 2.2)

It is also possible to write the emergent radiation from a star in the same terms as in section 2.1 with τ_μ as a scale of depth:

$$I_\nu^+(\tau = 0, \mu) = \int_0^\infty S_\nu(t_\nu) \exp(-t\nu/\mu) \mathrm{d}t_\nu/\mu \tag{2.31}$$

this can be rewritten by approximation of the Source function as $S = \sum_{n=0}^{\infty} a_n \tau^n$, which leads to

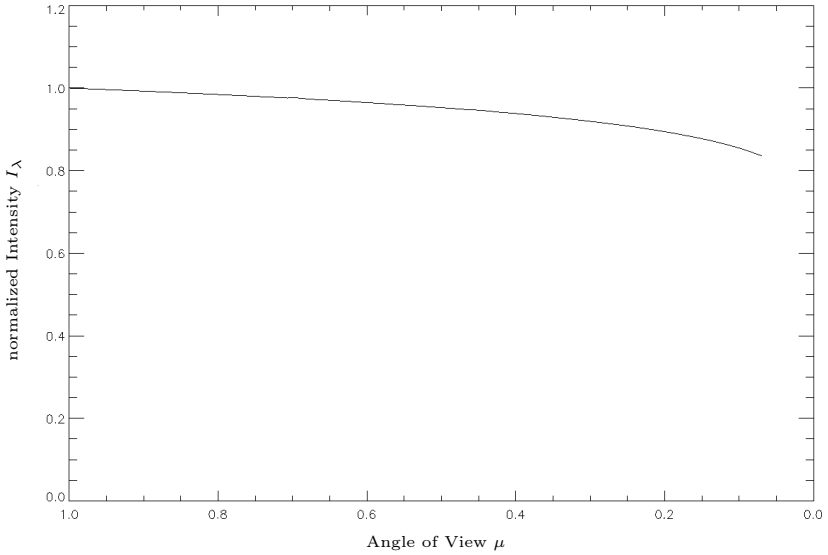

Figure 2.2: Center to limb variation of $I_\nu(\vartheta)$ for an arbitrary ν and a plane parallel test case, intensity is normalized to direct view of $I_\nu(\vartheta = 0°)$.

$$I_\nu^+(\tau = 0, \mu) = a_0 + a_1\mu + 2a_2\mu^2 + ... + n!a_n\mu^n \tag{2.32}$$

Truncation of S and I after the term of first order leads to the *Eddington-Barbier approximation*

$$I_\nu^+(\tau = 0, \mu) \approx S_\nu(\tau_\nu = \mu) \tag{2.33}$$

which leads to the same conclusion that the outgoing radiation is dominated by shallower levels at shallower angles of view with $\mu \longrightarrow 0$.

If we leave the 1D plane parallel ($\chi = \chi(z)$) or spherical symmetric ($\chi = \chi(r)$) case and allow for a three-dimensional one, where the opacity is $\chi = \chi\,(x, y, z)$, this effect can not be directly assumed. If χ_ν is still strongly z dependent, we can expect limb darkening to some extent, but as we will show later on, this is not generally the case in distinct structures with temperatures and opacities that vary strongly in lateral direction like the center of a starspot.

Chapter 3

Computational Method

This chapter gives an introduction to the implementation of 3D radiative transfer in the multi purpose stellar atmosphere code Phoenix that was used for the sunspot simulations in this work. The descriptions in this chapter are based upon the paperss of Hauschildt and Baron [2006, 2008, 2010], Baron and Hauschildt [2007] and Seelmann [2011].

The physical conditions are parametrized on a Cartesian, cylindrical or spherical voxel grid. In this work we used a Cartesian grid with $(2 \cdot n_x + 1) \times (2 \cdot n_y + 1) \times (2 \cdot n_z + 1)$ voxels, so that the voxel (0,0,0) is always at the grid center. We also applied periodic boundary conditions in x and y. Z is the direction perpendicular to the surface of the star. This set-up represents a semi infinite slab. In Cartesian coordinates, each voxel is an equally sized volume element $dV(ix, iy, iz)$ of the atmosphere with constant physical conditions inside the voxel, so that voxel size limits spatial resolution.

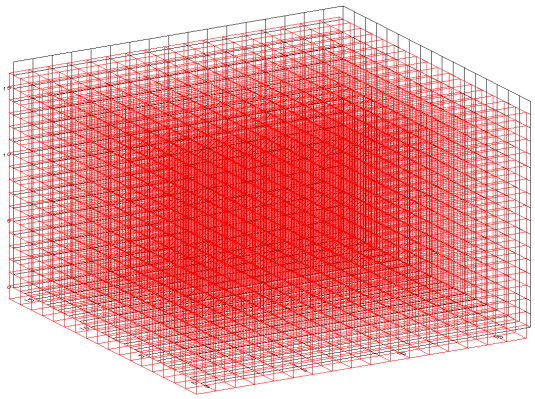

Figure 3.1: Voxel grid structure for a grid width $n_x = n_y = n_z = 8$ (4,913 voxel).

3.1 The Characteristics Method

Radiative transfer in Phoenix/3D is solved along characteristics. A characteristic is the mathematical representation of the geodesic a photon with a specific momentum travels along. This is similar to the characteristics method in 1D radiative transfer as described in chapter 2, but each characteristic is specified by two phase space angles (ϑ, ϕ) instead of just one.

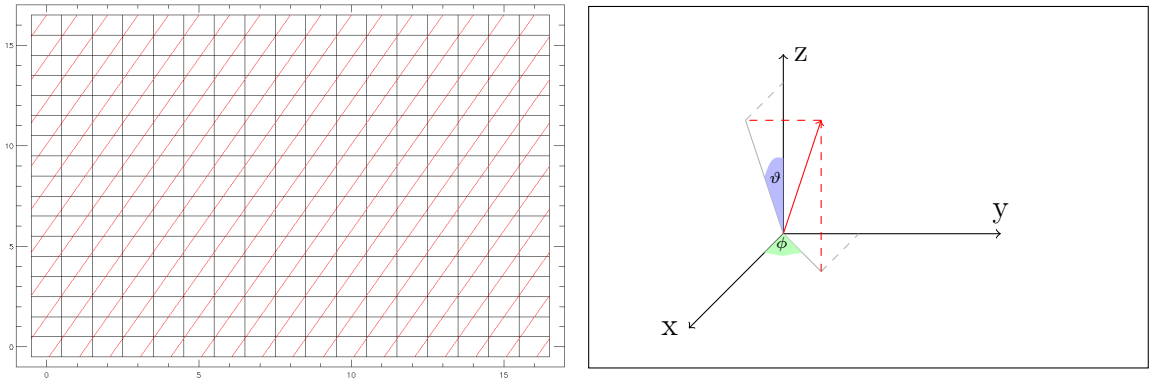

Figure 3.2: Left panel: Two dimensional projection in x-z plane of long characteristics tracked for one set of (ϑ, ϕ) in a Cartesian voxel grid with periodic boundary conditions (PBC). Right panel: Definition of ϑ and ϕ.

Here we use the full characteristics method (LC) where each characteristic is tracked starting from one of the boundary voxels at either $z = +n_z$ for incoming or $z = -n_z$ for outgoing characteristics trough the entire grid, as is shown systematically in figure 3.2 for a two dimensional slice of the grid. The periodic boundary conditions are applied by continuing any characteristic that leaves the grid at $\pm n_x$ or $\pm n_y$ at the opposite boundary of the grid at $\mp n_x$ or $\mp n_y$. Along each characteristic the formal solution, as defined in equation (2.10), can be computed by piecewise linear or piecewise parabolic interpolation and integration.

If we define the optical depth τ as optical depth along each characteristic, then the transport equation along a specific characteristic is simply

$$\frac{dI_\nu}{d\tau} = I_\nu - S_\nu \tag{3.1}$$

The optical depth along each characteristic depends on the opacities in the voxels that are crossed by the characteristic. Even two characteristics with the same phase space coordinates (ϑ, ϕ) may traverse different voxels, depending on their point of origin at the boundary. In the 1D plane parallel case, the phase space coordinates of each characteristic simply added a factor of μ to the optical depth, as was shown in (2.30). Here, we have to compute the formal solution for each characteristic individually.

It is possible to solve equation (3.1) for each optical depth point τ_i in the voxel grid along the characteristics, where $\tau_1 := 0$. The formal solution is then written as

$$I(\tau_i) = I(\tau_{i-1}) \cdot \exp(\tau_{i-1} - \tau_i) + \int_{\tau_{i-1}}^{\tau_i} S(\tau) \cdot \exp(\tau - \tau_i) d\tau \tag{3.2}$$

$$:= I(\tau_{i-1}) \cdot \exp(-\Delta\tau_{i-1}) + \Delta I_i \tag{3.3}$$

Assuming that the Source function S_i and the opacities χ_i for every point i of the voxel grid along the characteristic are already known, we can now calculate both $\Delta\tau_{i-1}$ and ΔI_i. The opacity between two optical depth points is interpolated linearly, which

leads to

$$\Delta\tau_{i-1} = \frac{(\chi_{i-1} + \chi_i) \cdot |s_{i-1} - s_i|}{2} \tag{3.4}$$

where s_i is the spatial path length along the characteristic and χ is the opacity per unit length.

For interpolation of the source function S_i we interpolate either linearly as well or parabolically and use

$$\Delta I_i = \alpha_i \cdot S_{i-1} + \beta_i S_i + \gamma_i S_{i+1} \tag{3.5}$$

where α, β and γ vary depending on the method of interpolation and were derived by Olson and Kunasz [1987]. In case of parabolic interpolation we have

$$\begin{aligned}
\alpha_i &= e_{0i} + e_{2i} - \frac{(\Delta\tau_i + 2\Delta\tau_{i-1}) \cdot e_{1i}}{\Delta\tau_{i-1} \cdot (\Delta\tau_i + \Delta\tau_{i-1})} \\
\beta_i &= \frac{(\Delta\tau_i + \Delta\tau_{i-1}) \cdot e_{1i} - e_{2i}}{\Delta\tau_{i-1}\Delta\tau_i} \\
\gamma_i &= \frac{e_{2i} - \Delta\tau_{i-1} e_{1i}}{\Delta\tau_i \cdot (\Delta\tau_i + \Delta\tau_{i-1})}
\end{aligned}$$

whilst for linear interpolation the coefficients are derived as

$$\begin{aligned}
\alpha_i &= e_{0i} - \frac{e_{1i}}{\Delta\tau_{i-1}} \\
\beta_i &= \frac{e_{1i}}{\Delta\tau_{i-1}} \\
\gamma_i &= 0
\end{aligned}$$

In both cases we used some supplementary functions which are defined as

$$\begin{aligned}
e_{0i} &= 1 - \exp(-\Delta\tau_{i-1}) \\
e_{1i} &= \Delta\tau_{i-1} - e_{0i} \\
e_{2i} &= (\Delta\tau_{i-1})^2 - 2 \cdot e_{1i}
\end{aligned}$$

As was shown in sections 2.3 and 2.4 we need the mean intensity J_i at every point of the grid to compute the full solution of the radiative transfer problem. Therefore we have to solve the solid angle integral numerically at each grid-point:

$$J = \frac{1}{4\pi} \oint_{4\pi} I(\vartheta, \phi) \cdot d\Omega = \frac{1}{4\pi} \int_0^{2\pi} \int_0^{\pi} I(\vartheta, \phi) \cdot \sin\vartheta \cdot d\vartheta \cdot d\phi \tag{3.6}$$

This integral is calculated by Monte-Carlo integration and therefore replaced by the Monte Carlo sum

$$J \cong \frac{1}{2\pi^2} \sum_{(\vartheta,\phi)} I(\vartheta, \phi) \sin(\vartheta) \tag{3.7}$$

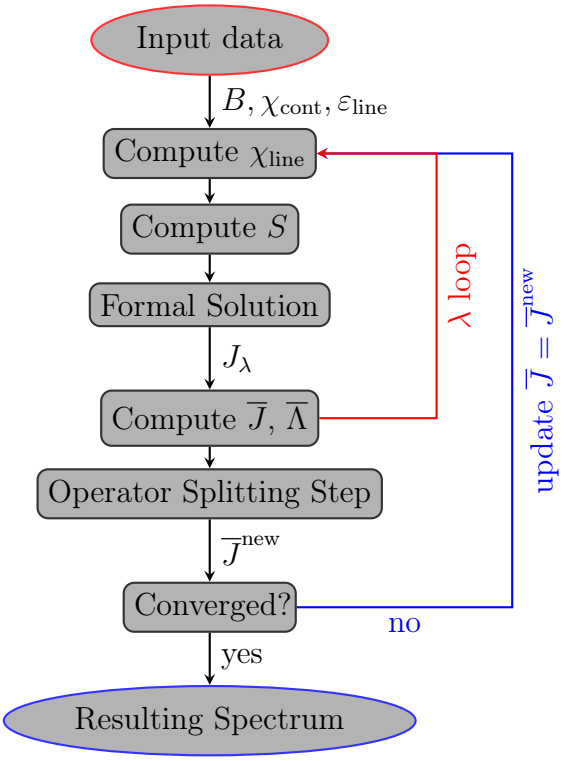

Figure 3.3: Structure of radiative transfer solution in 3DRT two level atom.

This summation is for every characteristic (ϑ, ϕ) that passes through the voxel it is calculated for. The phase space coordinates (ϑ, ϕ) for the characteristics can either be selected randomly, as is typical for Monte Carlo methods, or preselected if the number of characteristics is high enough to sample the whole solid angle space. In case of PHOENIX /3D we use a number of $n_\vartheta \times n_\phi$ evenly distributed characteristics.

3.2 The two level atom

For the first tests we used a simple two level atom configuration, simulating a single absorption line of variable center wavelength λ_0, variable width $\Delta\lambda$ and variable line strength x inside the periodic Cartesian grid. A plane parallel set-up is used for both opacity and temperature structure. This structure was modified by incorporating the temperature deviations for the sunspot models as described in section 4.3.

The line opacities are calculated from the continuous opacity, a free parameter x called *line strength* and the line profile function $\phi(\lambda)$ as

$$\chi_{line}(\lambda) = x \cdot \chi_{\text{cont}}(\lambda) \cdot \phi(\lambda) \tag{3.8}$$

In terms of radiation transport, this solver is capable of NLTE calculations with a source function consisting of LTE thermal emission plus complete redistribution scattering. This goes back to the works of Avrett [1965], who published an analytical solution for NLTE two level atoms with complete redistribution scattering.

Here, complete redistribution means that we do not assume coherence, yet the line

profil of the absorption of photons is equal to the line profil for the reemission of photons:

$$\phi_\lambda = \phi_\lambda^{\text{absorption}} = \phi_\lambda^{\text{emission}} \tag{3.9}$$

so that, in this case, the redistribution function $R(\lambda', n'; \lambda, n)$ is not a simple delta distribution. Instead, we allow scattering within the complete line profile $\phi(\lambda)$ of the transition. This means that it is possible to rewrite the emission by scattering as defined by equation (2.13), into

$$j_\lambda^{\text{scattering}} = \sigma_\lambda \oint_{4\pi} \int_0^\infty I_{\lambda'} \cdot \phi(\lambda') \cdot d\lambda' \tag{3.10}$$

This is different from coherent scattering as discussed in section 2.3 in such a way that the wavelength integral does not cancel out. This means that the emission by scattering is not proportional to J_λ, but to the mean intensity integrated over the whole line profile $\overline{J}$.

In the following, it is possible to use a similar scheme as described in 2.3, so that we can again define a source function for the line as

$$S_\lambda^{\text{line}} = (1 - \varepsilon_\lambda^{\text{line}})\overline{J} + \varepsilon_\lambda^{\text{line}} B_\lambda \tag{3.11}$$

The radiative transfer is solved by a combination of formal solution by characteristics method and an implementation of the operator splitting method. In this case, due to the use of complete redistribution, it is necessary to modify the iteration scheme and replace Λ_λ^* with $\overline{\Lambda}^*$, which is defined as

$$\overline{\Lambda}^* = \int_0^\infty \Lambda_\lambda^* d\lambda \tag{3.12}$$

The iteration is accelerated further by use of Ng's acceleration method, as described in Ng [1974]. The schematic of the radiative transfer solution of the two level solver is presented in figure 3.3.

For the simple test without change to the opacity structure, we used a grey temperature structure with $T_{\text{eff}} = 10000\text{K}$, and an optical depth range of $\tau \in [10^{-4}, 10^4]$. Both the planck function B and opacity χ were interpolated for each z layer of the grid. Each voxel was then modified according to the sunspot models for the temperature from section 4.3 thereafter. The results are discussed in section 5.1.

3.3 LTE Atom

By using the line strength as a single free parameter throughout the grid we omit the effect that three dimensional structures within our grid have on the opacity χ, which was so far assumed to be constant in x and y. Of course it would have been possible to introduce another free parameter and adjust the opacity as we did with the temperature, but since this would mean externally setting the number density for each species, we would of course not be able to attain any knowledge about the effects that the presence of a sunspot has on the composition of the stellar atmosphere inside the spot.

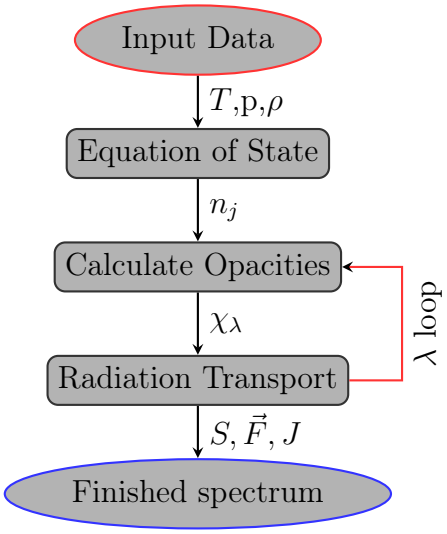

Figure 3.4: Flow chart for PHOENIX/3D stellar atmosphere simulation.

To address this problem, we need to solve the *equation of state* (EOS) for the entire voxel grid, so that we have the occupation numbers for each ionisation state of each species for each voxel depending on the temperature $T(x, y, z)$ and the pressure $p(x, y, z)$ inside the voxel. In the case of PHOENIX, the EOS is solved by the ACES module [Barman et al.], based on Smith and Missen [1982]. Here, we assume an LTE population of each level and ionisation stage, as given by equation (2.11). The line opacity at wavelength point λ for the transition $l \longrightarrow u$ can be written as

$$\left[\kappa_\lambda^l\right]^{\mathrm{LTE}} = \frac{\pi \cdot e^2}{m_e \cdot c} \cdot n_l^{\mathrm{LTE}} f_{lu} \left[1 - \exp\left(-\Delta E/(kT)\right)\right] \cdot \phi(\lambda - \lambda_0) \tag{3.13}$$

where n_l^{LTE} is the LTE population density of l, f_{lu} is the oscillator strength of $l \longrightarrow u$ and ϕ is the line profile, which is usually given by a Voigt function:

$$\begin{aligned} H(a, v) &\approx \mathrm{e}^{-v^2} + \frac{a}{\sqrt{\pi} v^2} \\ v &= (\lambda - \lambda_0)/\Delta\lambda \\ a &= \frac{\lambda^2 \gamma}{4\pi c \Delta\lambda} \end{aligned} \tag{3.14}$$

See e.g. Rutten [2003]. Since a Voigt profile is a convolution of a Gaussian function and a Lorentz profile γ, it can be approximated with a Gaussian shaped profile:

$$\phi\left(\lambda - \lambda_0\right) = \frac{1}{\pi \Delta\lambda} \mathrm{e}^{-((\lambda - \lambda_0)/\Delta\lambda)^2} \tag{3.15}$$

The total opacity can now be calculated by considering all transitions that are relevant at a given wavelength point and summation over all line opacities. Theoretically, both Voigt profile and Gaussian profile shaped lines would contribute to opacity for all wavelength points. However, the contribution at wavelength points far from the line center at λ_0 is extremely small, due to the shape of the profile functions. Therefore, we consider only lines within a certain wavelength range to limit the computational demands of the problem.

The EOS is solved for each voxel of the grid, the opacities are then calculated accordingly. Once the opacities for all voxels are known, the radiative transfer for the grid is solved. Here we use coherent and isotropic scattering as described in section 2.3, so that the transfer problem can be solved for each wavelength point individually by operator splitting. See figure 3.4 for a schematic of the program.

For our sunspot simulations, we used a PHOENIX/1D model for a solar type star with $T_{\text{eff}} = 5700$ K, and $\log(g) = 4.5$ as input data, which was taken from Hauschildt and Baron [2010]. Here, we used the temperature structure given by the model to build a plane parallel set-up, which was mapped onto our voxel grid. The resulting plane parallel structure was then modified according to our simple starspot models as described in section 4.3.

This temperature structure, together with the opacities calculated by solution of the equation of state, where used in a second series of calculations with the two level solver. This calculation featured both the opacity structure for a single line as well as total redistributive scattering.

Chapter 4

Modelling Sunspots

A *sunspot* or *starspot* is a region of the stellar surface, which has a lower surface intensity I than the rest of the stellar disk and is thus perceived as a dark patch. Starspots are known to be cooler by several thousand Kelvin compared to the so called quiet surface of star.

To calculate the effects of starspots on the stellar atmosphere and the stellar spectrum, we have created a simple model of a starspot and solved the radiative transfer problem in three dimensions. A starspot has a complicated structure where the temperature T, and, therefore, the chemical composition and, of course, the opacity χ as well, depends on all three spatial coordinates. For this reason, a 1D model and 1D solution of radiative transfer is not sufficient to model a starspot.

This chapter gives a brief introduction into formation and physical properties of starspots and details in which way these properties were implemented into a simple model of a spot inside the framework of our 3D stellar atmosphere simulation code. The descriptions of starspots and their formation are based upon the work of Thomas and Weiss [2008], Chitre [1963] and references therein.

4.1 Formation of Sunspots

Sunspots are caused by the stellar magnetic field. This is the reason for the fact that the sun is not constantly covered by the same number of spots, even though individual spots might be longliving. The solar magnetic field is constantly changing during a 22 years cycle between two recurrences of the same polarity. The number of sunspots on the other hand has a cycle of about 11 years between two maxima. During the solar maximum, a large number of spots can be observed on the stellar surface, while the solar surface is almost bare of spots during the solar minimum. Furthermore, the regions in which spots can be found depends on the solar cycle as well. We can see a migration of few spots at the solar equator during solar minimum to many spots near the solar poles during solar maximum - though it is of course not individual spots that migrate, but the region in which they are formed.

A spot forms in a region, where magnetic field lines penetrate the solar surface with high field strength of several thousand gauss and cause a reduction in convective energy transport. The field lines of the solar magnetic field are in motion while the solar magnetic field is slowly reverting its polarity, therefore, the regions where field lines can penetrate the surface slowly migrates. This explains the shift of the principal spot regions over the

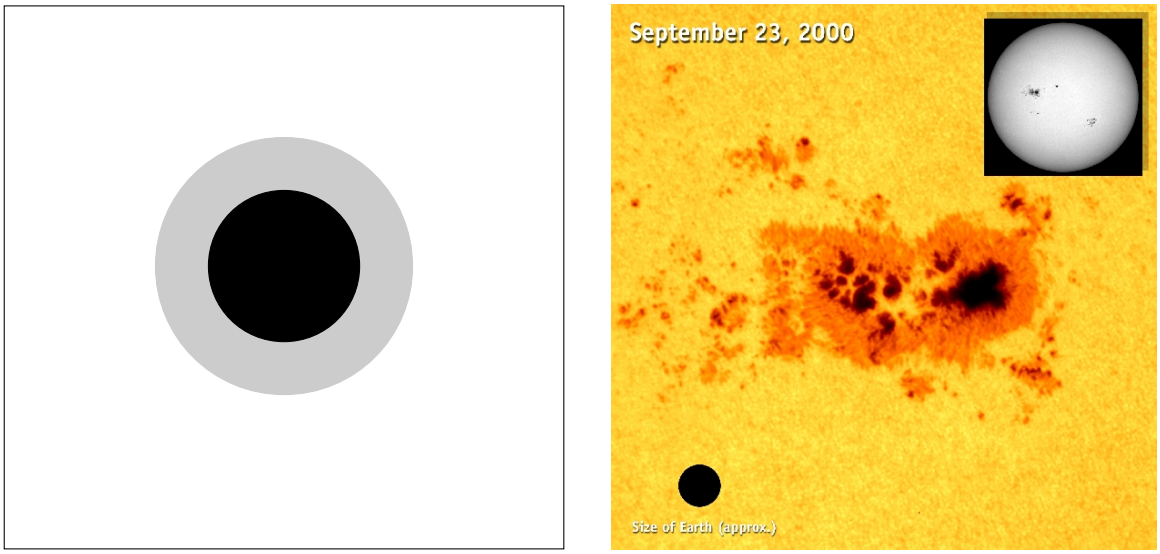

Figure 4.1: Left: Schematic representation of a sunspot with dark umbral core (black) and penumbra (grey). Right: Real image of a group of sunspots on the solar surface, courtesy of SOHO (ESA & NASA).

solar cycle.

The formation process itself usually takes place over several days. After the spot has fully formed, it begins to slowly decay back to the quiet level over a period of weeks and sometimes even up to a few months. During this time, the spot itself remains fairly stable over an extended period of time, though, of course it is not actually completely static.

In the region, where the magnetic field lines break through the solar surface, the convective energy transport is partially suppressed by the magnetic field so that the heat flux from the area below the sunspot towards the outside is considerably reduced. Furthermore, all convective motions within the sunspot itself are channelled along the magnetic field lines. Limited convective heat transport is possible, but not very effective. In this way the spot is largely thermally isolated from its surroundings since it is limited to radiation as a source of energy transport, thus reducing the rate at which energy can be transported up into the spot region.

4.2 Properties of Sunspots

Under close observation, a sunspot is revealed to be much more complex structure than just a uniform dark patch of the solar surface. It is common practice to distinguish between two different regions of the spot. The darkest inner part of the spot is called the *umbra*. It usually takes up around one third of the spots total area. Surrounding the umbra is the *penumbra*, which serves as a transition region between the dark inner parts of the sunspot and the bright quiet surface around it. The penumbra is still darker, than the quiet surface but not as dark, as the umbra. In many cases, the penumbra is very irregular in its shape, which most likely is influenced by the thermal structure of the surrounding atmosphere. The penumbra of several spots can be joined, so that a structure of several umbral cores within a single penumbra is created. Figure 4.1 shows

a schematic of the spot in its most simple representation as well as a real picture of a sunspot for comparison.

The entire sunspot of both, umbra and penumbra, combined, can have a diameter of several thousand kilometers. The actual size of spots varies greatly. Where the smallest spots are known to have a diameters of around 3500 km, the largest known spots have diameters of 60.000 kilometers or more, which corresponds to almost 0.1 percent of the solar surface.

The umbra of solar spots typically has a temperature between 1000 K and 2000 K cooler than the surrounding quiet surface. This difference in temperature is not constant over the entire height of the spot, but changes and of course finally drops to zero at the bottom of the spot. In terms of intensity, the umbra radiates only about 20 percent of the quiet sun intensity at its core and closer to 60 percent at the boundary to the penumbra. This boundary is a question of definition, since the actual transition is continuous.

The penumbra is between 250 K and 400 K cooler than the surrounding photosphere and has an intensity average of 75 percent of the quiet sun. In terms of area, it takes up the majority of the spots total area, though the exact border depends on the definition of the umbra-penumbra boundary. This area ratio is not a constant however, even with the same boundary the ratio still depends on the size of the spot, while smaller spots tend to have even smaller umbral sizes compared to the spot size.

4.3 Spot models

In this work we used static physical set-ups, simulating a spot that has already fully formed. As a first approximation, we introduced a region of lower temperature into our model of the stellar atmosphere to simulate the immediate effect that the sunspot has on the solar spectrum directly as well as indirectly.

For this work, we assumed that sunspots or starspots would be rotationally symmetric to the center of the umbra, so that the spot itself is a perfect circle, when seen from above ($\mu = 1$). Real sunspots are quite irregular in shape, so that this is, of course, an approximation. However, it would be impossible to account for any possible shape of spot without simulating the formation process. Besides, we are primarily interested in the effect the spot has on the spectrum and the rest of the atmosphere, therefore, the simple shape has the advantage of reducing the number of free parameters for the model and being easy to recognize in the shape of the resulting spot.

A sunspot with one or even two regions of constant temperature or constant relative temperature would obviously not be stable and any discontinuous drop in temperature causes strong effects at the position of the discontinuity. For this reason we used simple functions to simulate continuous transition between the temperature at the outside and the temperature at the core of the spot, so that the transitions between umbra, penumbra and quiet photosphere are as continuous as a discrete grid allows for.

The spot itself was structured so that it narrowed with increasing depth since spots obviously have a lower boundary determined by the point where temperatures reach the level of the quiet sun again.

Constant Model

For test purposes, we set up a simple cylindrical box of constant temperature T_{spot}, which is set between the depth z and $z+\Delta z$ and for distances from the grid center of $r_{xy} \leq r_{\text{spot}}$. This model served as a test setup for our solver and was the base for the developement of more complex models. A three dimensional structure cut of this simple test box can be seen in figure 4.2.

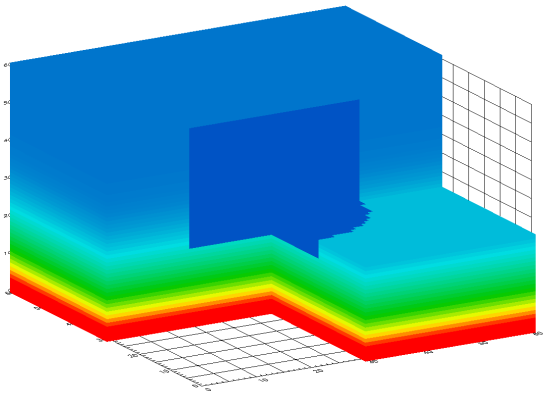

Figure 4.2: Constant test model, temperature structure in three dimensions.

Cylindrical Model

The first model that allows for a non constant temperature of the spot, affects the temperature on a cylindrical part of the upper stellar atmosphere. The temperature at the center of the cylinder is set constant to a value of $T_{\text{spot}} = T_{\text{pp}} - \Delta T_{\text{spot}}$, the temperature then increases exponentially depending on the radial distance r from the center of the umbra up to a distance r_{spot}, outside of which the normal plane parallel structure of the model grid is assumed. The spot is assumed to have a height Δz and begins at $z = z_{\text{min}}$, where z is the height above the bottom of the grid.

$$T(x,y,z) = T_{\text{pp}}(z) - \Delta T_{\text{spot}} \exp\left(-\left(\frac{r(x,y,z)}{r_{\text{spot}}}\right)^2\right) \quad \forall\, r \leq r_{\text{spot}} \wedge z \in [z_{\text{min}}, z+\Delta z] \tag{4.1}$$

where $r = \sqrt{x^2+y^2}$ and $T_{\text{pp}}(z)$ is the temperature of the plane parallel model. Likewise the spot is cut of at a maximum depth. The resulting temperature structure is shown schematically in figure 4.3 as cuts through the model grid.

Conical Model

Models with a maximum radius and depth cause a discontinuity in temperature, which would of course be thermally unstable. It seems more logical to have a structure that is larger on the surface, than in the lower parts of the atmosphere, thus beeing spatially compact without beeing discontinous. Therefore, the second model was set up as a non

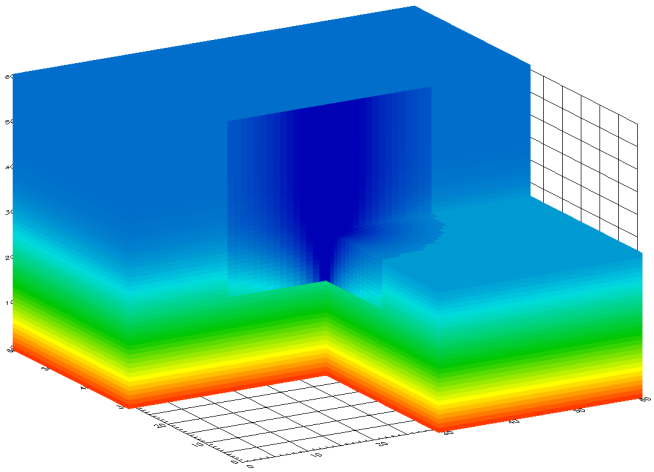

Figure 4.3: Cylindrical model, temperature structure in three dimensions.

regular cone with temperature gradients in both r and z direction. It begins at its full radius at the top of the atmosphere and reduces its radius as it proceeds into deeper layers according to

$$r_{\text{spot}}(z) = r_{\text{spot,max}}\sqrt{-\log(d(z)/d_{\text{max}})} \quad \vee \quad r_{\text{spot,max}} \text{ for } d(z) = 0 \tag{4.2}$$

where d in this case is the distance from the surface or $d = z_{\text{surface}} - z$ and d_{max} is the lower boundary of the spot. The temperature is calculated as

$$T(x,y,z) = T_{\text{pp}}(z) - \Delta T_{\text{spot}} \cdot \exp\left(-\left(\frac{r(x,y,z)}{r_{\text{spot}}(z)}\right)^2\right) \cdot \exp\left(-\frac{d(z)}{d_{\text{scale}}}\right) \tag{4.3}$$

where d_{scale} is a free parameter for control of the vertical temperature scale.

This model was implemented both into the two level solver, as well as the full PHOENIX-/3D program, for which the chemical composition of the atmosphere is calculated consistently. The resulting temperature structure is illustrated in figure 4.4, for different sets of parameters.

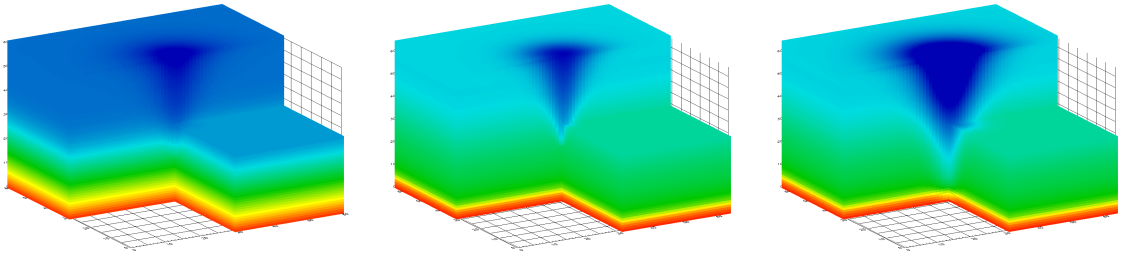

(a) 2 level model (b) PHOENIX3D shallow model (c) PHOENIX3D deep model

Figure 4.4: Conical model, schematic temperature structure for three different sets of parameters.

Chapter 5

Results

5.1 Temperature and Scattering Effects

In our first calculations, the temperature of the sunspot was lowered without considering a change to the opacity. The lower temperature means that the source function inside the spot region is lower, thus we can expect it to be darker even without an increase in opacity. Furthermore we expect non-zero flux-vector components in x and y direction due to the fact that the temperature gradient in the atmosphere is no longer parallel to $\vec{e}_z$ since we departed from the conditions of a plane parallel atmosphere.

In this case, the models were calculated for a grid structure with $n_x = n_y = n_z = 30$, and therefore a total number of 226 981 voxels, where each single voxel represents a cubical element of volume with $a_{\text{voxel}} \approx 16.39\text{km}$, and a total size of the computational domain of $a_{\text{grid}} = 1000\text{km}$.

Constant Model

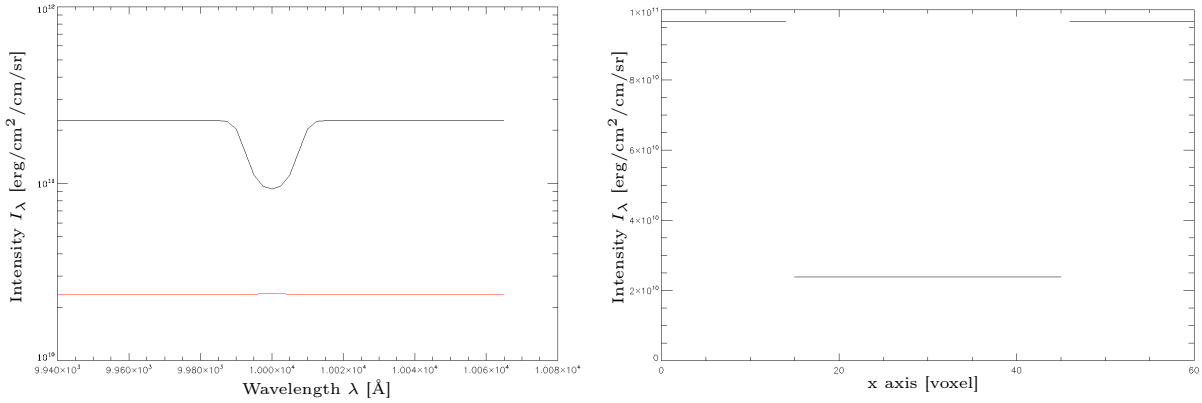

(a) Spectrum (b) Lateral profile

Figure 5.1: Constant model, left panel: Intensity for the spectrum above the spot (red) and for the quiet surface (black). Right panel: Lateral profile through the center of the grid.

First, we tested the 3D radiative transfer simulation program by calculating the radiation field inside a simple structure with a cylindrical zone of constant temperature T,

as introduced in section 4.3. As could be expected from this extremely simple model, all surface voxels of the spot show a constant intensity, since huge parts of the grid below have a constant temperature. As can be seen in figure 5.1b, the discontinuity in temperature is reproduced in the lateral profile, where we see a jump from the quiet intensity outside to the reduced intensity inside at the boundary of the anomaly.

In this calculation, the spot model is positioned in the center of the grid and does not reach up to the top. For this reason, the line center is not affected as much, as the continuum, since the line is due to its higher opacity, generated at shallower depth, so that it does not see as much of the spot. The result is that the absorption line vanishes above the anomaly and is replaced by a very weak emission feature, as can be seen in figure 5.1a.

If we take a look at the flux in a two dimensional cut, shown in figure 5.2a, we find a huge deviation from the z direction at the edges of the anomaly, where the temperature discontinuity is located. The flux is redirected more strongly in the lower parts of the atmosphere, where the outside temperature and, therefore, the temperature difference is higher. Respectively, there is almost no flux in the center of the spot, where there is no temperature gradient at all.

For obvious reasons, this configuration does not cause a spot with a clear distinction between umbra and penumbra, but a simple dark patch on the surface, as seen in figure 5.2b. However, these are exactly the results we expected from a simple configuration like this, therefore we have successfully tested our solver.

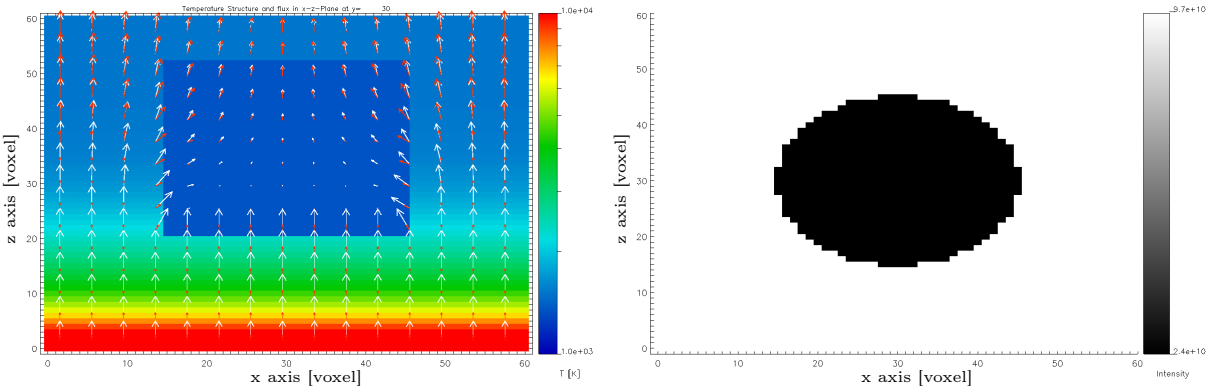

(a) Temperature and Flux

(b) Surface Intensity

Figure 5.2: Constant model, left panel: Temperature and x and z components of the flux as vectors in a plane through the center of the spot. Line flux $\vec{F}(\lambda_{\text{line}})$ is drawn in red, while continuum flux $\vec{F}(\lambda_{\text{cont}})$ is drawn in white. The temperature T of each voxel is shown as background color. Right panel: Visualisation of the surface intensity $I_\lambda(\lambda = \lambda_{\text{line}})$ for a characteristic of $(\vartheta, \phi) = (0, 0)$.

Cylindrical Model

With the results of the first tests in mind, we have replaced the constant temperature settings with a simple cylindrical model with temperature gradients, as has been described

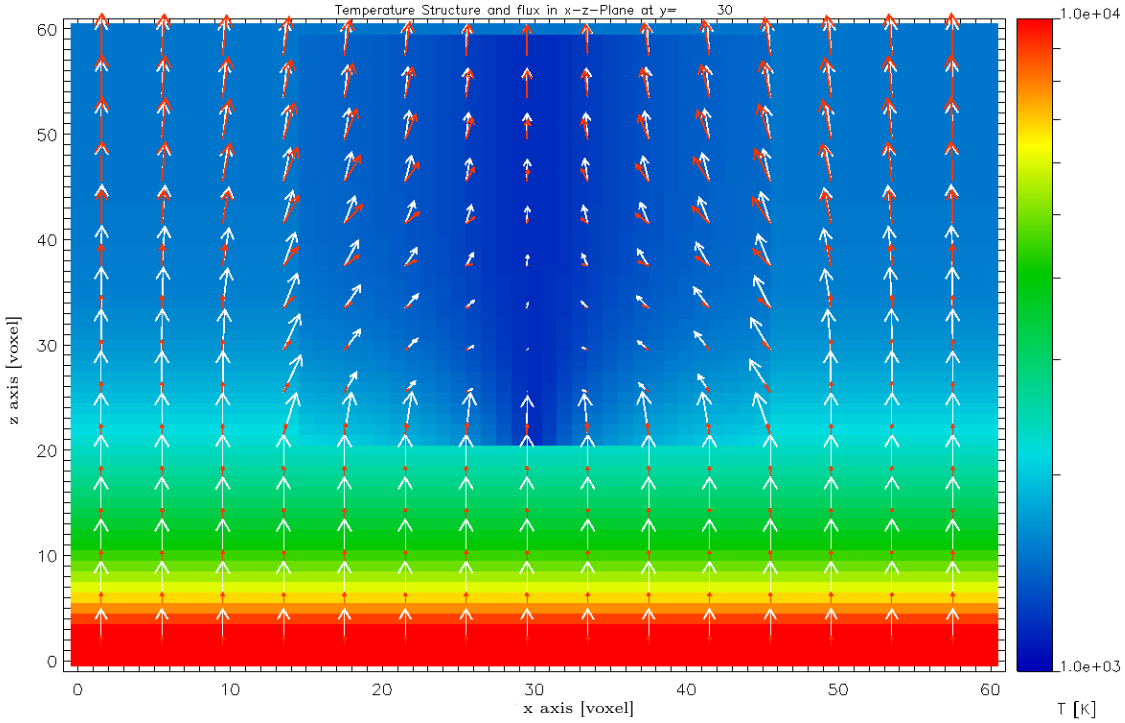

Figure 5.3: Cylindrical spot model, temperature and flux in a plane through the center of the spot. Line flux $\vec{F}(\lambda_{\text{line}})$ is drawn in red, while continuum flux $\vec{F}(\lambda_{\text{cont}})$ is drawn in white. The temperature of each voxel is shown as background color.

in section 4.3. In this model the temperature is lowest in the upper center of the spot. The temperature difference

$$\Delta T(x, y, z) = |T(x, y, z) - T_{pp}(z)|$$

where T_{pp} is the temperature of the plane parallel structure, is reduced exponentially towards the rim of the spot with a steeper gradient in deeper layers. The spot still features discontinuities in temperature at its maximum diameter and even more so at its lower boundary.

The following parameters where set for the spot model as defined by section 4.3:

$$\begin{aligned} T_{\text{spot}} &= 4000\text{K} \\ r_{\text{spot}} &= 250\text{km} \\ z_{\text{min}} &= 350\text{km} \\ \Delta z &= 650\text{km} \end{aligned}$$

Figure 5.3 shows both temperature structure and the flux in x and z directions in a x-z cut through our grid at $y = 30$ and, therefore, trough the center of the umbra, where no flux in y direction is expected due to the cylindrical symmetry of the model.

We can still see the effect of the temperature discontinuity at the spots boundaries. The flux is redirected into the spot, and the redirection is again most pronounced where the temperature gradient is high, e.g. at the discontinuous lower boundary. This is most

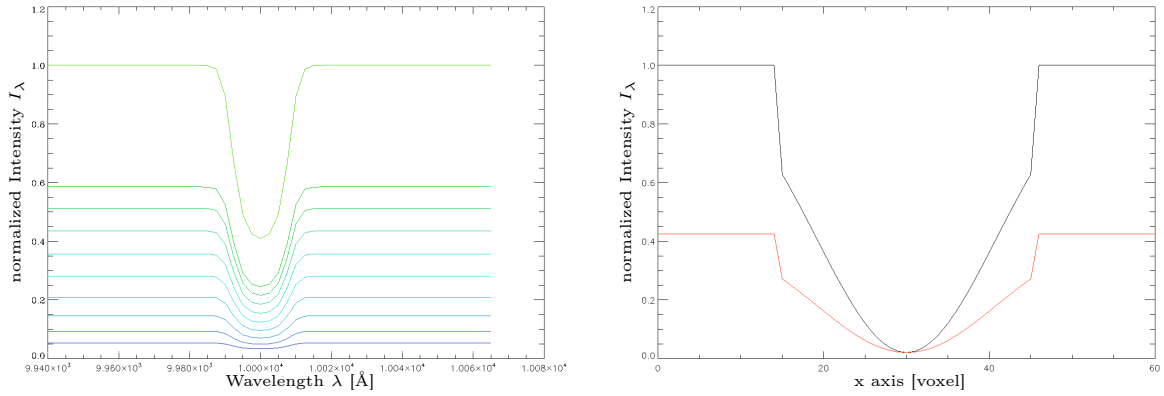

Figure 5.4: Cylindrical spot model, right: Spectra of surface voxels from the quiet sun (green) to the center of the umbra (blue) along a diagonal of the voxel grid. Intensity is normalized to quiet continuum intensity. Right panel: Intensity at $\lambda = \lambda_{\text{line}}$ (red) and $\lambda = \lambda_{\text{continuum}}$ (black) for a lateral profile at the surface of the grid.

discernible in the continuum where the changes in flux are negligible outside the spot. There is still almost no flux in the center of the spot, where the temperatures are more or less constant.

Furthermore, the spot has a greater influence on the flux at the line centre, where it is redirected more strongly by the same temperature gradient. Since the atmosphere is optically thicker at the line than at a continuum point, this as not too surprising since optically thin structures have less influence on the emerging spectrum.

In figure 5.4 we see the change in intensity along a diagonal of the grid surface. As before, the effect of the spot is stronger in the continuum, since the temperature difference is higher at the bottom end of the grid. Just as in the constant test model, we do not see the line in the umbral spectrum. Furthermore, we can see that the line weakens in the outer regions of the spot. Since we have implemented a transition between the outside and the inside of the spot, this could be expected.

In this test case, the umbra is 4000K cooler than the quiet grid at its center, this results in a drop in intensity to below 20 percent of the quiet continuum for the umbra and about 20 to 60 percent for the penumbral region. The drop in line intensity is not nearly as strong, but this is of course due to the fact that the opacity change due to the lowered temperatures has not been considered yet.

Of course we are interested in the spot as it would be visible at the surface, therefore we computed the formal solution for a view directly from above with $(\vartheta, \phi) = (0, 0)$. As shown in figure 5.5 for different wavelengths, the model has produced a spot with a distinctive difference between umbral and penumbral region. Using $I = 0.75 \cdot I_{\text{quiet}}$ as limit between umbra and penumbra, we have an umbra to penumbra ratio of about

$$\frac{A_{\text{umbra}}}{A_{\text{spot}}} = \mathbf{0.4}$$

However, we see a non continuous drop by almost 40 percent in intensity at the rim of the spot, which is obviously due to the use of a maximum diameter of the spot and the resulting discontinuity in temperature at this radius.

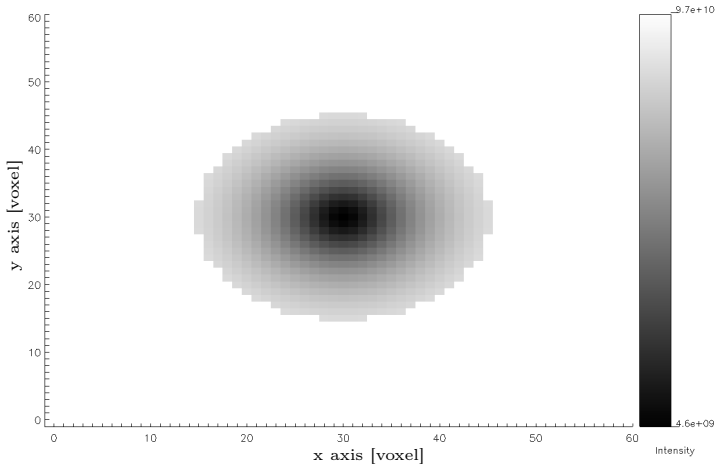

Figure 5.5: Cylindrical spot model, intensity as seen from above the spot, color coded logarithmically from $4.6 \cdot 10^9$erg/cm^2/cm/sr (black) to $9.7 \cdot 10^{10}$erg/cm^2/cm/sr (white).

Conical model

So far, we have seen that the calculation is strongly affected by discontinuities in the temperature structure. For this reason, we have set up another model, in which we ventured to remove these and replace them by smooth transitions. In this model the temperature difference is reduced exponentially in z and r so that we see a conical shape. This change applies to the entire grid in r, so that there is no discontinuity but those generated by the discretization of the grid. There is still a discontinuity in temperature at the lower boundary due to the finite size of the voxels inside which the temperature is constant, though it is not as pronounced as before. The parameters as defined in the full description of the model in section 4.3 were set up as follows:

$$\begin{aligned} T_{\text{spot}} &= 4000\text{K} \\ r_{\text{spot}} &= 250\text{km} \\ d_{\max} &= 700\text{km} \\ d_{\text{scale}} &= 800\text{km} \end{aligned}$$

so that this model is equal in size to the previous model at the surface.

In figure 5.6 the temperature structure and flux are shown for a vertical cut through the center of the simulated spot. In this case, the flux is diverted from the z direction where the temperature gradient is steepest and stronger for the line than for the continuum. Without the temperature discontinuity at the rim of the spot, the effects of the rim of the spot are not as strong. However, there is still some effect in the lowest affected voxel at the bottom of the spot, where the temperature is not discontinuous, but the gradient from one voxel to its neighbours is steep.

The reduction in surface intensity, compared to the quiet surface, is not as pronounced in this spot, mainly because the temperature difference between the center of the umbral region and the quiet sun is lower at greater depth than in the previous model. In figure 5.7 we show that the continuum intensity is lowered to around 80 percent in the penumbra and down to just below 50 percent in the umbra. The darkening is still stronger in the continuum, than in the line, since we yet have to account for opacity effects.

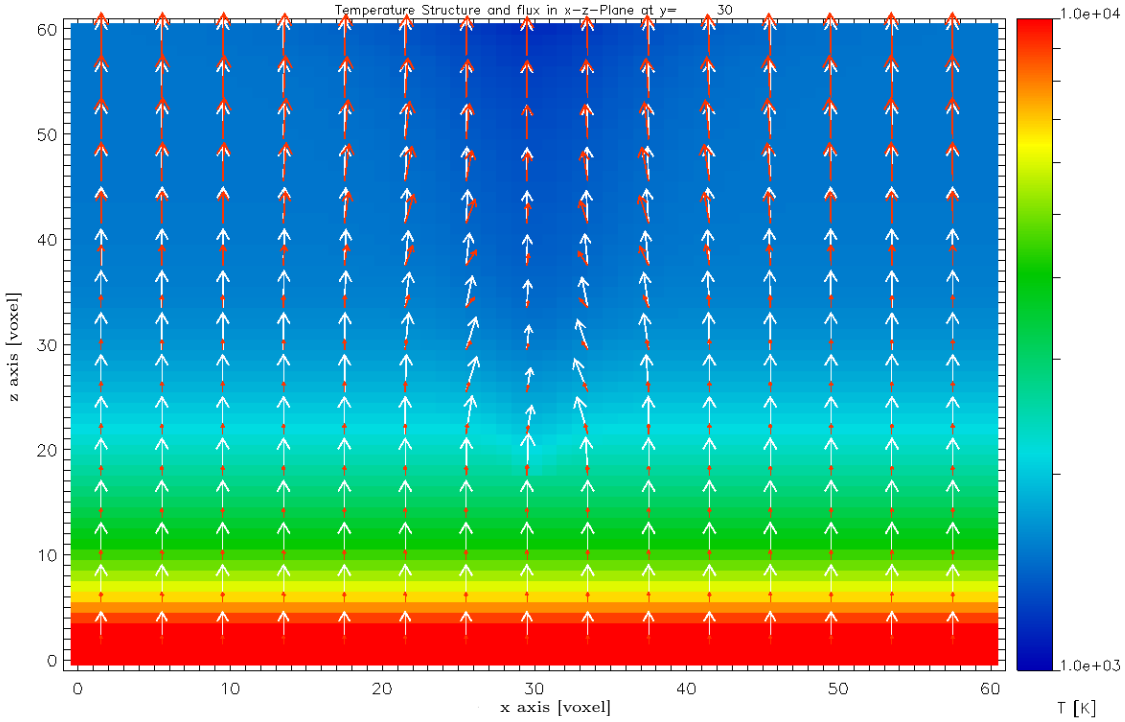

Figure 5.6: Conical spot model: Temperature and flux in a plane through the center of the spot. Line flux $\vec{F}(\lambda_{\text{line}})$ is drawn in red, while continuum flux $\vec{F}(\lambda_{\text{cont}})$ is drawn in white. The temperature of each voxel is shown as background color.

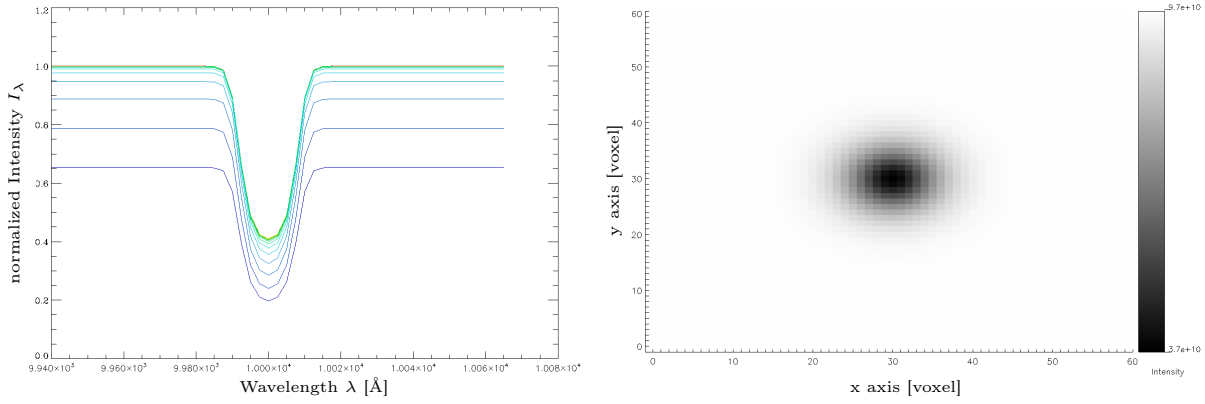

Figure 5.7: Conical spot model, left panel: Surface voxel spectra from the quiet sun (green) to the center of the umbra (blue) along a diagonal of the voxel grid. Intensity is normed to quiet continuum intensity. Right panel: Intensity at $\lambda = \lambda_{line}$ for the surface of the grid, color coded logarithmically from $3.7 \cdot 10^{10}$erg/cm^2/cm/sr (black) to $9.7 \cdot 10^{10}$erg/cm^2/cm/sr (white).

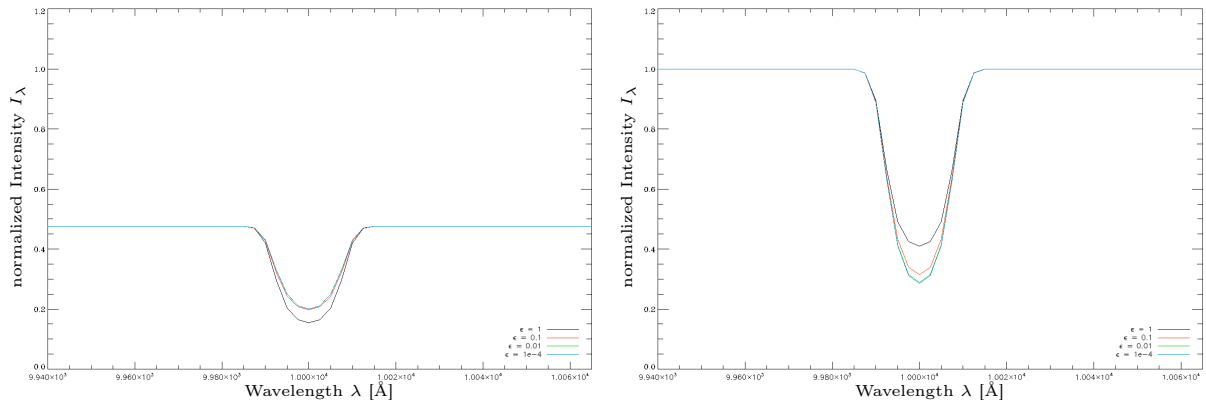

Figure 5.8: Conical model: Intensity spectrum for different scattering coefficients $\varepsilon_{\text{line}} = 1, 0.1, 0.01, 0.0001$, left: above the spot, right: at the edge of the grid, normalized to quiet continuum level.

On the surface, this spot appears to be considerably smaller than the first spot, with a higher ratio of umbral area to penumbral area of:

$$\frac{A_{\text{umbra}}}{A_{\text{spot}}} \approx 0.3$$

with $I = 0.75 \cdot I_{\text{quiet}}$ as border between umbra and penumbra. This is a result of the inclusion of additional temperature gradients. Despite the fact that the spot is spread farther on the surface without a strict outer boundary to the quiet atmosphere, the region that has the lowest temperature is smaller. This is caused by the temperature gradient in z direction.

Scattering

At this point, we used the same conical model but included line scattering with complete redistribution, as described in section 3.2. In this case, we used line thermal coupling parameters of $\varepsilon_{line} = 0.1,\ 0.01$ and 0.0001 as defined by equation (3.11). Scattering connects spatially distant parts of the atmosphere, so that we expect to see an effect of interaction between the cooler spot and the quiet atmosphere surrounding it.

Figure 5.8 shows the intensity spectrum for the surface voxel above the spot and for another surface voxel at the edge of the grid for different grades of scattering. For increased influence of scattering, the line depth in the region above the spot is reduced while we see a deepening of the line in the region around the spot. The scattering, thus, reduces the effect of the lower temperature in the immediate vicinity of the spot, but increases the area of effect, thus enlarging the darkening of the solar surface.

To examine this effect more closely, we plot the intensity at the line center λ_{line}, where the change due to scattering is most obvious, as a lateral profile over the grids x axis. Figure 5.9 shows that the visible spot has indeed grown in size, but is less dark as well. The outer boundary has grown slightly, while the darker part of the penumbra as well as the umbra moved farther inwards. This means that the observed spot is actually larger than the zone of reduced temperature suggests, because scattering spreads the total loss

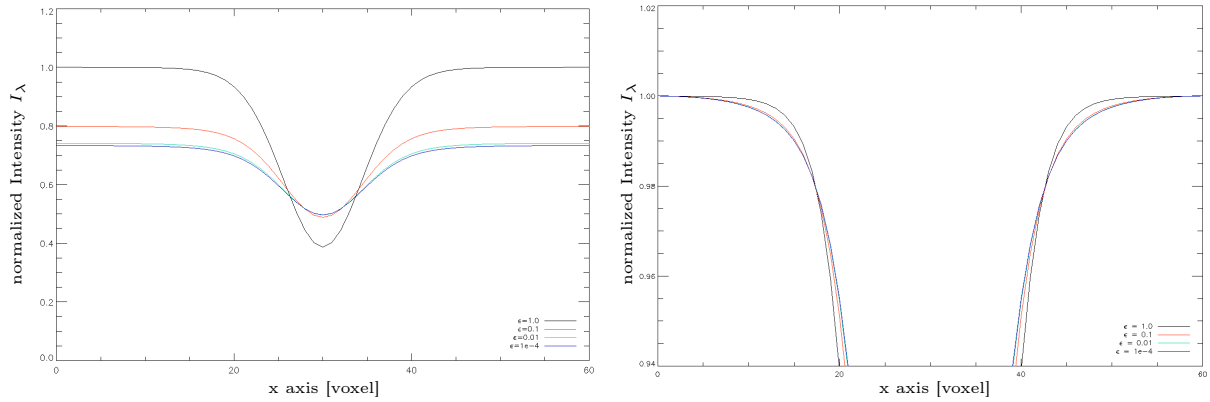

Figure 5.9: Surface intensity along a lateral profile through the center of the spot at $y = 30$, $\lambda = \lambda_{\text{line}}$ for different $\varepsilon_{\text{line}} = 1, 0.1, 0.01, 0.0001$. Left panel: normalized to quiet non-scattering continuum intensity, right panel: normalized to quiet line of each case for comparison of spot size.

of intensity over a larger area.

The redistribution of photons into the darker spot is seen even better if we take a look at the scattering calculations for the first model in figure 5.10. In this model, the reduction of the temperature is strong enough to black out the center of the umbra almost completely to only a few percent of the quiet continuum level. With line scattering we see emission features, which of course are generated by the photons that are scattered into the spot. Figure 5.10b illustrates how the darkening of the stellar atmosphere is spread beyond the region where the spot affects the temperature structure of the atmosphere, as even parts of the lateral profile that are outside the spot region, which is limited to a maximum radius in this model, are darkened. In this case, the discontinuity actually helps to point out this effect.

Figure 5.11 shows the flux in x-z plane for different scattering coefficients $\varepsilon_{\text{line}}$. Here, we see that scattering reduces the influence of the spot, as the flux is not redirected into the spot as much, as in the case without scattering. The changes are large in the upper part of the atmosphere, but small at the lower end of the spot model.

5.2 Carbon Monoxide in Sunspots

We have shown the influence the reduced temperature inside the spot has by itself without consideration of the effect this change in temperature has on the equation of state and therefore the opacities in our atmosphere. We have expanded our model calculation to incorporate the latter effect. Since we are interested in the formation of molecules in the cooler regions of a sunspot, we need to allow for a change in the chemical composition of the atmosphere. We have lowered the temperature, therefore, we expect an increased concentration of molecules such as CO.

The model we use is again conically shaped, so that we may compare our results with the test case of the two level atom. We begin by using a model for the solar atmosphere as

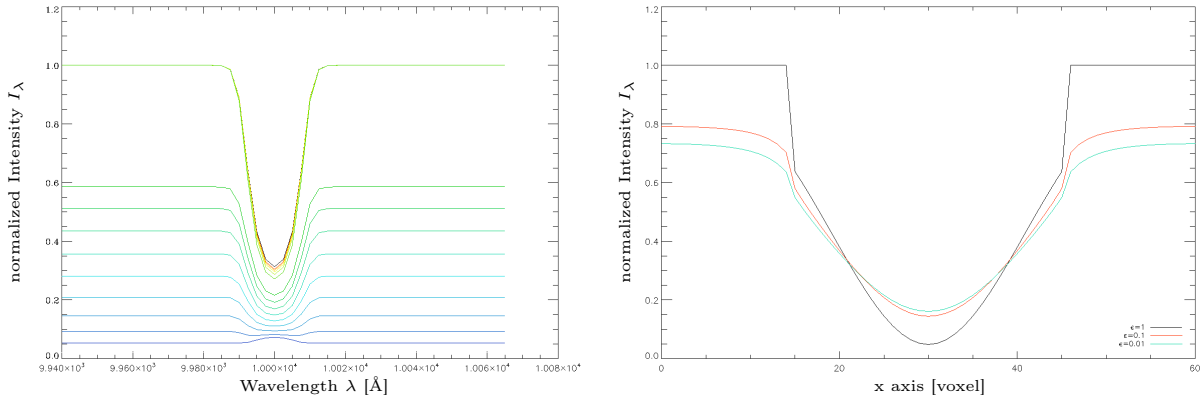

(a) Spectra (b) Lateral profile

Figure 5.10: Cylindrical model with scattering, left panel: surface voxel spectra from the quiet sun (red/green) to the center of the umbra (blue) along a diagonal of the voxel grid. $\varepsilon_{\text{line}} = 0.1$ Intensity is normed to quiet continuum intensity. Right Panel: Lateral profiles at $\lambda = \lambda_{\text{line}}$ for $\varepsilon_{\text{line}} = 1, 0.1$ and 0.01, intensity is normalized to non scattering quiet line level.

	shallow model	deep model
ΔT_{spot}	-2000K	-2000K
r_{spot}	250km	350km
d_{max}	900km	1800km
d_{scale}	1000km	2000km

Table 5.1: Model parameters for the conical PHOENIX3D sunspot models.

a base for a plane parallel model and again incorporate local changes to the temperature in the center of the grid. For the model parameters, see table 5.1.

In this case, all calculations were done for a grid structure with $n_x = n_y = n_z = 32$ and a total number of 274 625 voxels. Each single voxel represents a cubical element of volume with an edge length of $a_{\text{voxel}} \approx 22.4$km, which gives the entire grid a total edge length of $a_{\text{grid}} = 1455$km.

Figure 5.12 shows a color coded plot with the opacity structure from a vertical x-z cut through the atmosphere. We can see that the opacity inside the spot model is increased by several orders of magnitudes for some wavelength points, while only negligible for others. Furthermore, the shape of the region of changing opacity is wavelength dependent as well.

This is not very surprising, since the opacity is changed by the presence or absence of various atomic and molecular species. We see huge changes, where a major contributor to opacity at a wavelength point is able to exist due to a favourable temperature and small or no changes in regions where the species that dominate the opacity for this wavelength points are little or not affected by the change of temperature, for instance because the respective lines are generated in different layers of the atmosphere.

We can test this hypothesis easily by plotting the CO concentration inside our atmosphere. Figure 5.13 shows both the absolute CO concentration in parts per million, and the increase in CO concentration compared to the quiet solar atmosphere. The structure

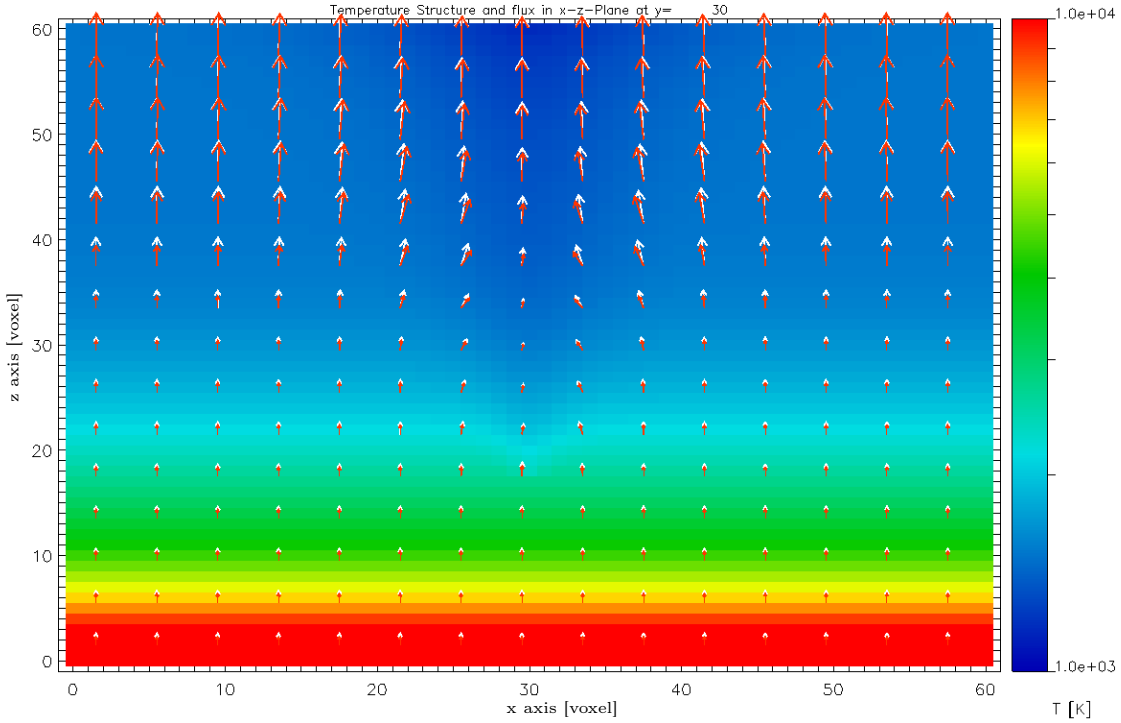

(a) $\varepsilon_{\text{line}} = 10^{-1}$

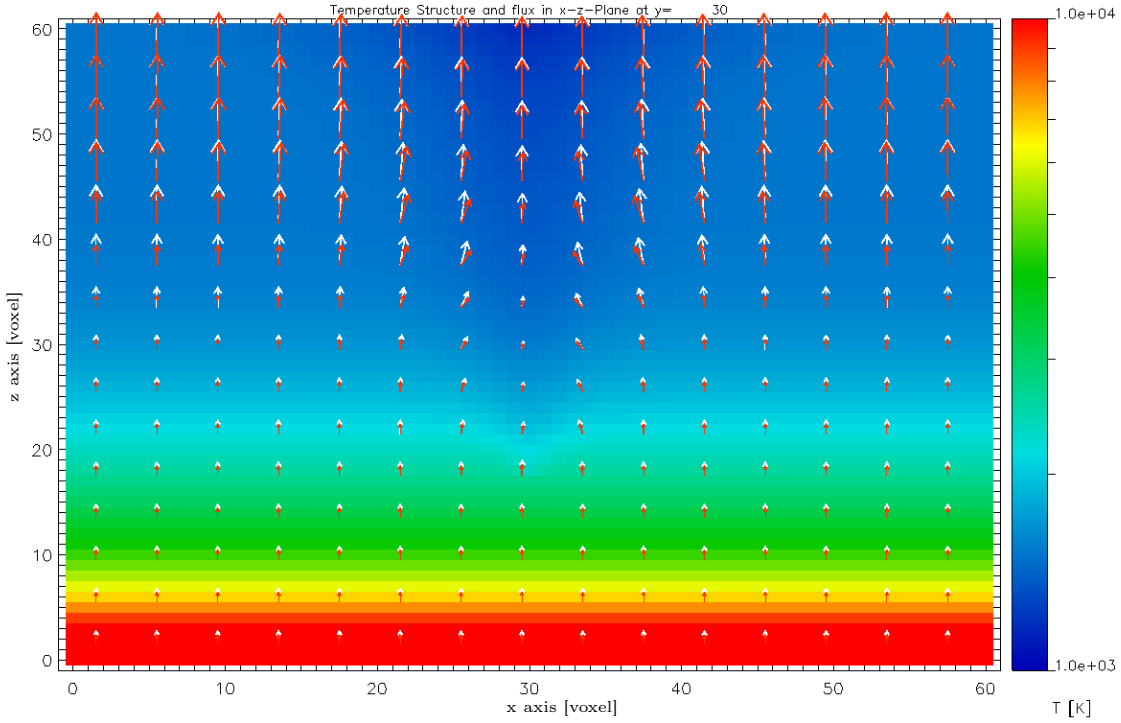

(b) $\varepsilon_{\text{line}} = 10^{-4}$

Figure 5.11: Conical model with different scattering coefficients $\varepsilon_{\text{line}}$ with flux $\vec{F}(\lambda_{\text{line}})$ shown in red, compared to flux $\vec{F}(\lambda_{\text{line}})$ of case without scattering $\varepsilon_{\text{line}} = 1$ (white). Each vector in the graph represents the average over 4×4 voxels. The color of the background shows the Temperature T of each voxel.

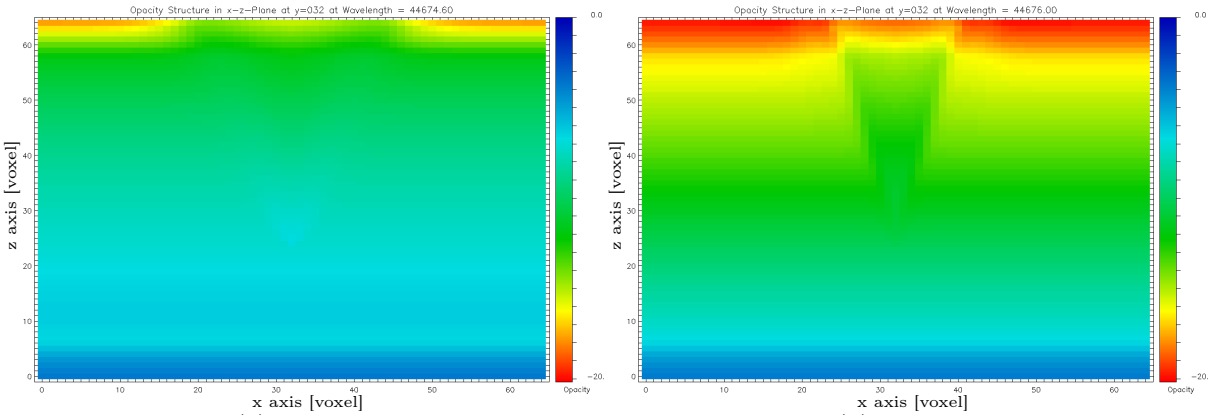

(a) $\lambda = \lambda_{\text{line}}$ (b) $\lambda = \lambda_{\text{cont}}$

Figure 5.12: Opacity structure in x-z plane, calculated from the shallow conical model in a solar type atmosphere. Difference between opacities for the line and the continuum. Opacity χ color coded logarithmically from 10^{-20}cm^{-1} to 10^{0}cm^{-1}.

of the spot can be seen quite clearly as a region of comparatively high CO concentration, with the highest concentration in the cool core of the spot. In the right panel, we find that at the surface of the spot, the CO concentration is almost 20.000 times higher than in the undisturbed parts of the atmosphere. Furthermore, we see that the change to the CO concentration is high at the surface and the bottom of the spot, where in the quiet atmosphere there is little or no CO present. If we compare this plot to the opacity structure of a CO line in figure 5.12, the region of highest change to CO concentration is, of course, the same region that has the highest change to opacity.

In comparison to the plane parallel model we used for our two level calculations, the model for the atmosphere of a G-type star we used here has a less steep vertical temperature gradient and the upper region we are interested in is optically thinner than before. Thus, the first result we obtain is that the effect on the continuum is almost non existent if we use similar model parameters for the sunspot as in the test environment of the two level solver, as shown in figure 5.14. This makes sense, if we consider that molecules like CO can only exist where the temperature is low enough, so it is only natural that the CO lines we are looking at emerge in the upper atmosphere and, therefore, are a much better tell-tale for temperature changes in this region, than the continuum, for which the local medium is optically thin. Figure 5.15 shows the relative line opacity of a CO line with $\lambda_{\text{line}} = 44674.6$ Å and the CO concentration in the atmosphere for the pure plane parallel case. We see that for this atmospheric model, CO molecules are only formed in the upper part of the atmosphere, in the same reason, where our spot model resides.

Since our model spots have been tiny compared to known real sunspots so far, we set up a second model with the same structure, but increase both the diameter and the depth untill which the sunspot affects the atmosphere. The opacity structure for this model is shown in figure 5.16. Besides the obvious increase in size at the surface, which is due to the increased diameter of the spot, we can see that the change in opacity at the lower end is more pronounced within the line, and the continuum. If we look again at the change in

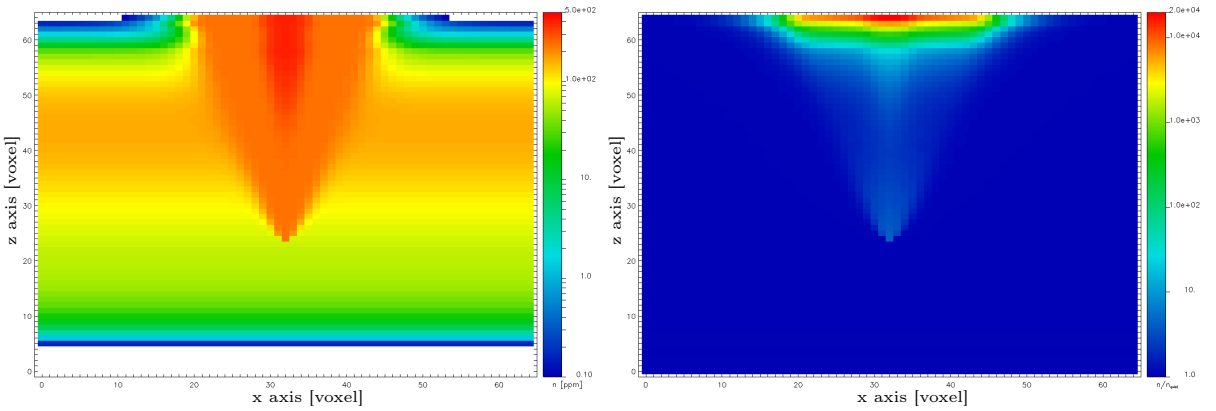

Figure 5.13: Effect of the shallow sunspot model on the formation of Carbon Monoxide (CO) in stellar atmospheres. Left panel: CO concentration in parts per million, color coded from 0.1 ppm (blue) to 500 ppm (red). Right panel: relative CO concentration compared to undisturbed atmosphere $\frac{n_{\mathrm{CO}}}{n_{\mathrm{CO}}^{\mathrm{quiet}}}$, color coded from 1 (blue) to 20000 (red).

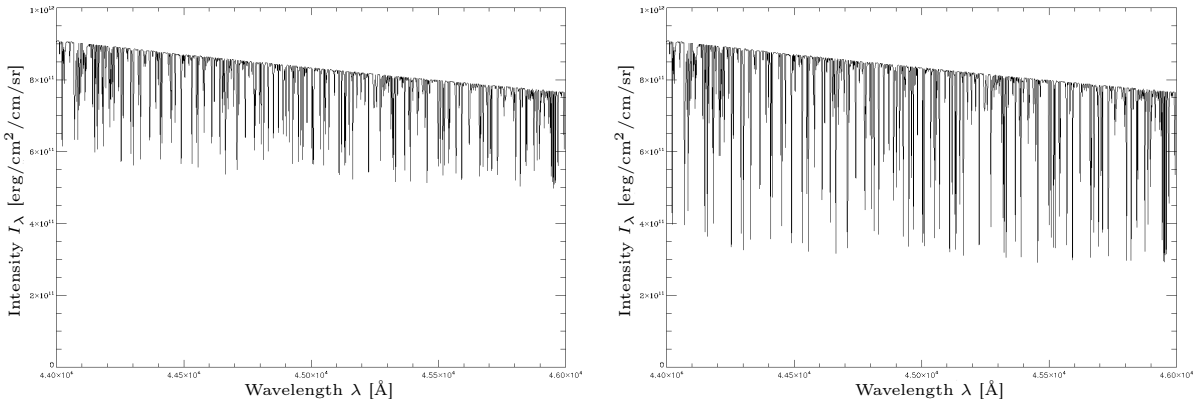

(a) Quiet Sun (b) Umbra

Figure 5.14: Shallow model: CO Band Spectra between 44000 Å and 46000 Å for the quiet surface (left) compared with the umbral center (right).

CO concentration for this model, which is done in figure 5.17, we can see the reason for this immediately. The lower temperature at the bottom of the spot allows for creation of CO in a region that would be almost bare of it without the sunspot. In this way, the relative increase is huge, even though not as high as at the surface.

If we take a closer look at figure 5.18, which shows the temperature structure of an x-z cut through the grid and has markings for the $\tau = 1$ level of both line and continuum wavelength points, we can see, the different effect on CO lines and continuum directly. In the shallow model, the continuum is dominated by radiation from a depth that is far beyond the lower boundary of the spot model, so that the spot is entirely in the optically thin region of the atmosphere and thus affects the outgoing radiation very little. Even at an affected line wavelength point, where the increased opacity in the sunspot reduces the depth of the $\tau = 1$ level locally, the spot is barely in the CO line forming region of the atmosphere and the darkening is dominated by the increased opacity, not by the reduced

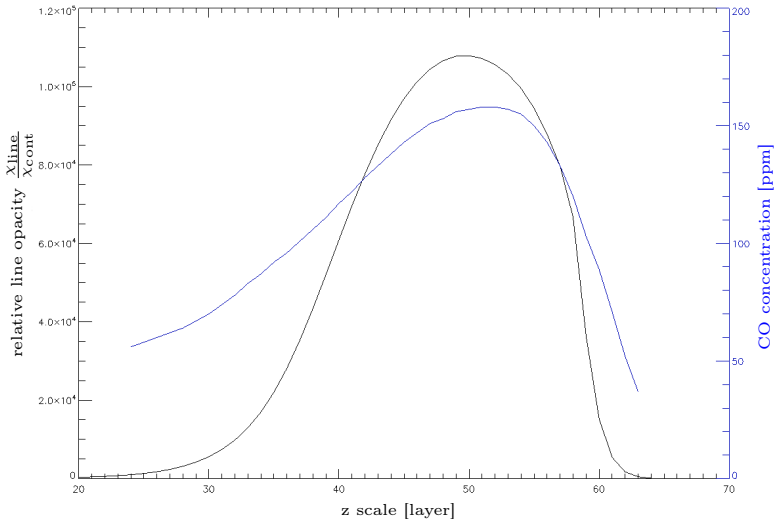

Figure 5.15: Relative line opacity $\frac{\chi_{line}}{\chi_{cont}}$ for the CO line $\lambda_{line} = 44674.6$ Å (black) and CO concentration of the plane parallel atmospheric model in parts per million (blue).

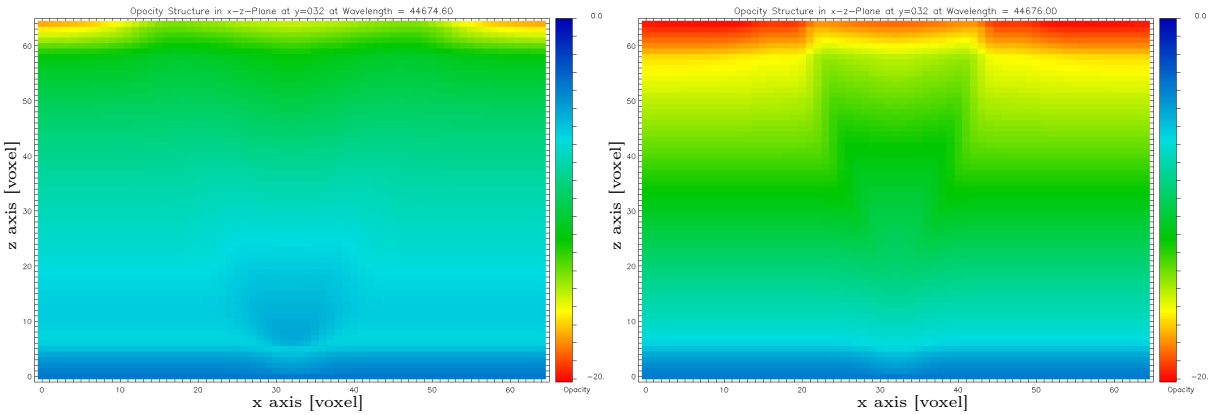

(a) $\lambda = \lambda_{line}$ (b) $\lambda = \lambda_{cont}$

Figure 5.16: Opacity structure in x-z plane, calculated for the deep model for a wavelength point at the line center and a continuum point. Opacity χ color coded logarithmically from 10^{-20}cm^{-1} to 10^{0}cm^{-1}.

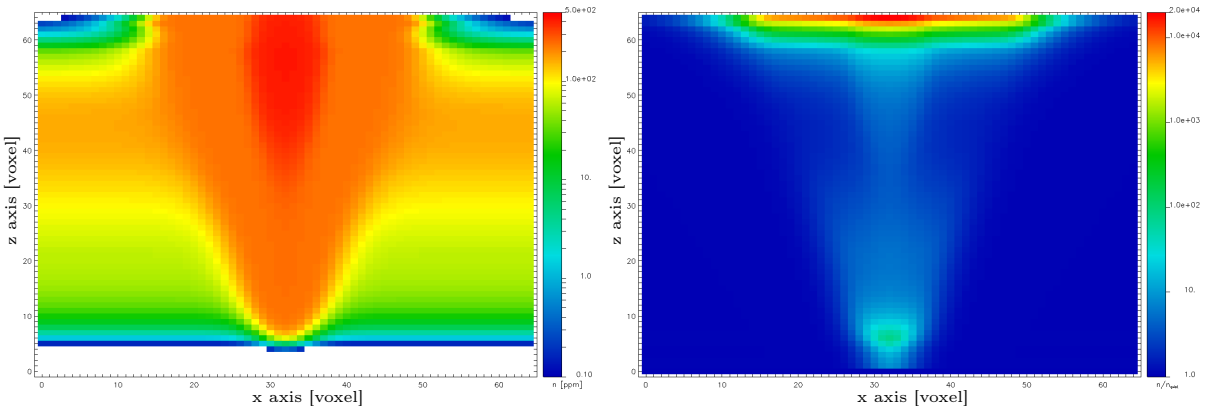

Figure 5.17: Effect of the deep sunspot model on the formation of Carbon Monoxide (CO) in stellar atmospheres. Left panel: CO concentration in parts per million, color coded logarithmically from 0.1 ppm (blue) to 500 ppm (red). Right panel: relative CO concentration compared to undisturbed atmosphere $\frac{n_{\mathrm{CO}}}{n_{\mathrm{CO}}^{\mathrm{quiet}}}$, color coded logarithmically from 1 (blue) to 20000 (red).

temperature directly.

In the deep spot model, as shown in figure 5.18b, we see a different behaviour. Again the affected line opacity lowers the depth of the $\tau = 1$ level and shows us colder regions of the atmosphere. This time however, the effect spreads farther out and is much more visible. The continuum level is affected as well. Even though the reduced opacity allows for a deeper look into the atmosphere, we see only the lower part of the spot, which is still cooler than the level we would see in the quiet part of the atmosphere. Therefore, the continuum intensity is reduced as well, though not by as much as at the line center. In this, we can see an obvious difference to the shallow model, as illustrated by the spectra for the deep model in figure 5.19.

Influence on different CO bands and atomic lines

We have set up two different models of sunspots with different sizes. Furthermore, we have shown that even a shallow spot has a strong influence on line opacities that are generated by molecules in the upper part of the atmosphere, because the reduced temperature increases the number of molecules that form and the size of the region, in which formation is possible. However, we must not forget that it is as of yet not possible to resolve a starspot by observation *directly*. Therefore, it is of interest, to investigate how the changes to temperature and opacity would affect the stellar spectra. The spectra in figures 5.14 and 5.19 show parts of the CO band spectrum with $\Delta\nu = 1$ for both models. We have already seen that they are strongly affected by the presence of the sunspot.

For comparison, we have produced another spectrum for the shallow model for the $\Delta\nu = 2$ band spectrum, which is shown in figure 5.20. Here, we see that while the band spectrum again shows stronger lines than the quiet surface, the darkening is not as pronounced, and not all lines seen are affected. Blueward of the band head at 23000Å, we see that few lines are affected at all. The unaffected lines are atomic lines like Fe I and Mg I, which originate at a lower level of the atmosphere. This spot model is shallow and we already saw that it does not effect the continuum. The not affected lines are, therefore,

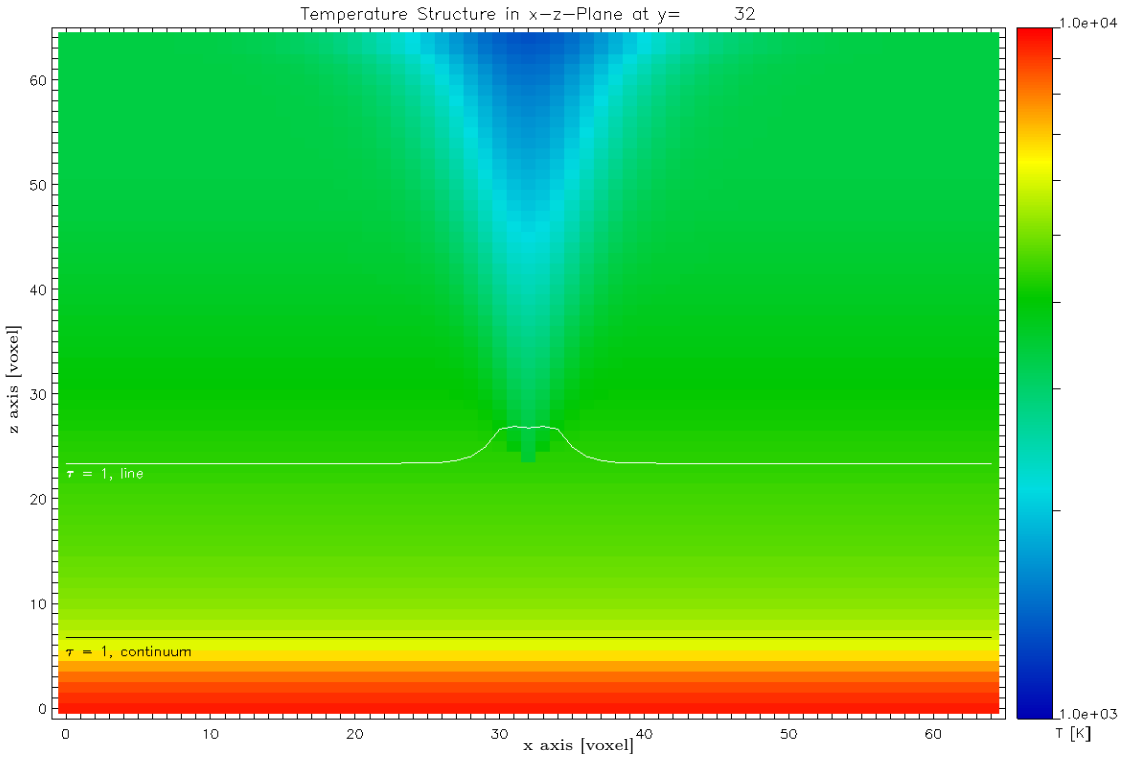

(a) Shallow model

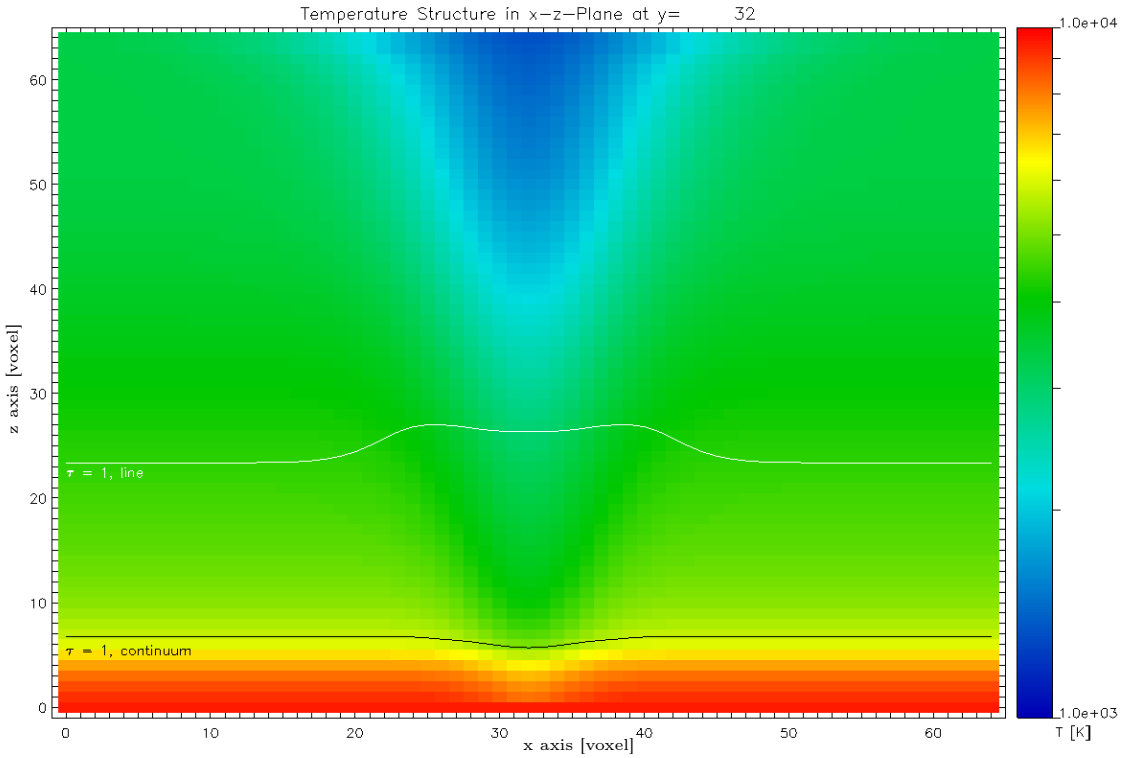

(b) Deep model

Figure 5.18: Temperature structure for the *shallow model* (upper panel) as well as the *deep model* (lower panel). Temperature is shown color coded logarithmically from 1000 K to 10000 K. The white lines mark the optical depth $\tau = 1$ for $\lambda = \lambda_{\text{line}}$, while the black lines mark the optical depth $\tau = 1$ for $\lambda = \lambda_{\text{cont}}$ along characteristics with $(\vartheta, \phi) = (0, 0)$.

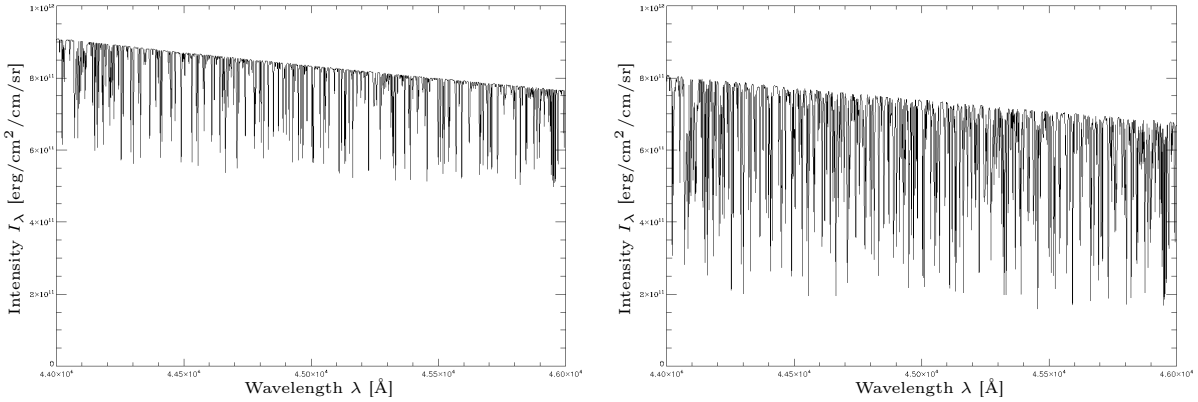

(a) Quiet Sun (b) Umbra

Figure 5.19: Deep model: $\Delta\nu = 1$ CO band spectrum between 44000Å and 46000Å for quiet sun (left) compared with umbral center (right).

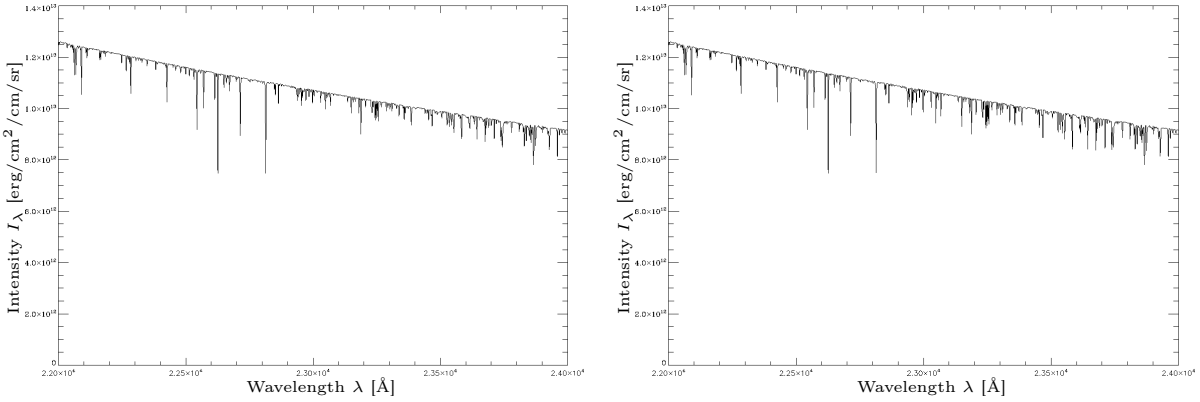

(a) Quiet Sun (b) Umbra

Figure 5.20: Shallow model: CO Band Spectra with $\Delta\nu = 2$ between 22000Å and 24000Å for the quiet surface (left) compared with the umbral center (right).

those that are formed in a lower region of the stellar atmosphere as well, as we can see from the the $\tau = 1$ level, plotted in figure 5.22 for a not affected Mg I line at $\lambda = 22816$ Å. In the case of the line shown, the opacity is even reduced in the spot region.

Moreover, lines that are already strong are more strongly affected than those which are faint on the quiet surface. However, if we compare the absolute darkening of the CO lines in both bands, as was done in figure 5.21, we see that the absolute darkening in the band at 23,000Å is greater, than in the 4µm band. This is not surprising, since the overall intensity in the 2µm band is more than one order of magnitude higher.

5.3 Center-to-limb variation of Sunspots

As we have described in section 2.5, the apparent brightness of the solar disk varies from the center to the limb. This effect is commonly known as *limb darkening*. This is true only for the quiet sun and the mean brightness of any part of the solar surface that is

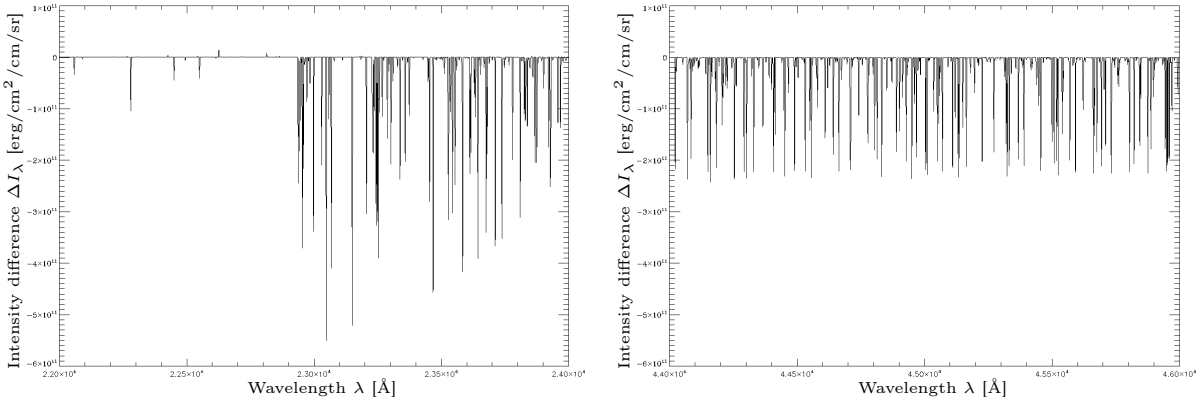

(a) $\Delta\nu = 2$ band (b) $\Delta\nu = 1$ band

Figure 5.21: Shallow model: Darkening of the Umbra, shown as Intensity difference between umbra and quiet surface $\Delta I_\nu = I_\nu^{\text{umbra}} - I_\nu^{\text{quiet}}$ between 22000Å and 24000Å (left panel) as well as 44000Å and 46000Å (right panel).

large against the size of the three dimensional structures, especially sunspots.

Our model calculations show that the opposite is true for a sunspot structure, which appears less dark, if observed close to the edge of the solar disk. In case of sunspots we, thus, have *limb brightening* instead of limb darkening. This effect is visible in the images shown in figure 5.23, which panels represent color coded plots of the intensity at the surface of our voxel grid for a single wavelength and angle of view, and figure 5.24, which shows the intensity I_ν at line wavelength $\lambda = \lambda_{\text{line}}$ of the darkest voxel of the spot compared to a reference voxel far outside the spot plotted over angle of view μ.

We have already discussed the reason for limb darkening in section 2.5 for the plane parallel case. The sunspot is, of course, breaking the symmetry of the underlying plane parallel structure since the opacities seen along a specific characteristic are not independent of the beginning of the characteristic on the surface of the star. If we look at the sunspot directly from above, all characteristics that pass through the sunspot traverse its entire structure from the lowest boundary up to the top (see figure 5.25). However, if we look at a spot from a point above the rim of the grid, we see the spot through a characteristic with $(\vartheta, \phi) \neq (0, 0)$. This characteristic does not traverse the entire spot from bottom to top but only part of it. This effect is increasing the farther we depart from the direct view from the top.

The increased opacity inside the spot reduces the atmospheric depth to which we can see, so that the spot usually appears darker than its surrounding, as shown in figure 5.25 where the lower black line marks the level of $\tau = 1$ for all characteristics. If we now increase the angle of view, the characteristics that pass through the center of the spot at its lower end do not traverse the upper regions of the spot at all, but a region of lower opacity outside the spot. Since this effect is different for each characteristic and angle, the shape of the $\tau = 1$ line begins to change, so that we see different parts of the spot. The spot itself is smeared out because every characteristic passing through it only traverses a fraction of it. The darkest region of the spot gets brighter. (See figure 5.26)

Figure 5.24 points out that the spot brightening peaks between at about $\mu = 0.2$ depending on the model and, consequently, remains fairly constant in relative brightness

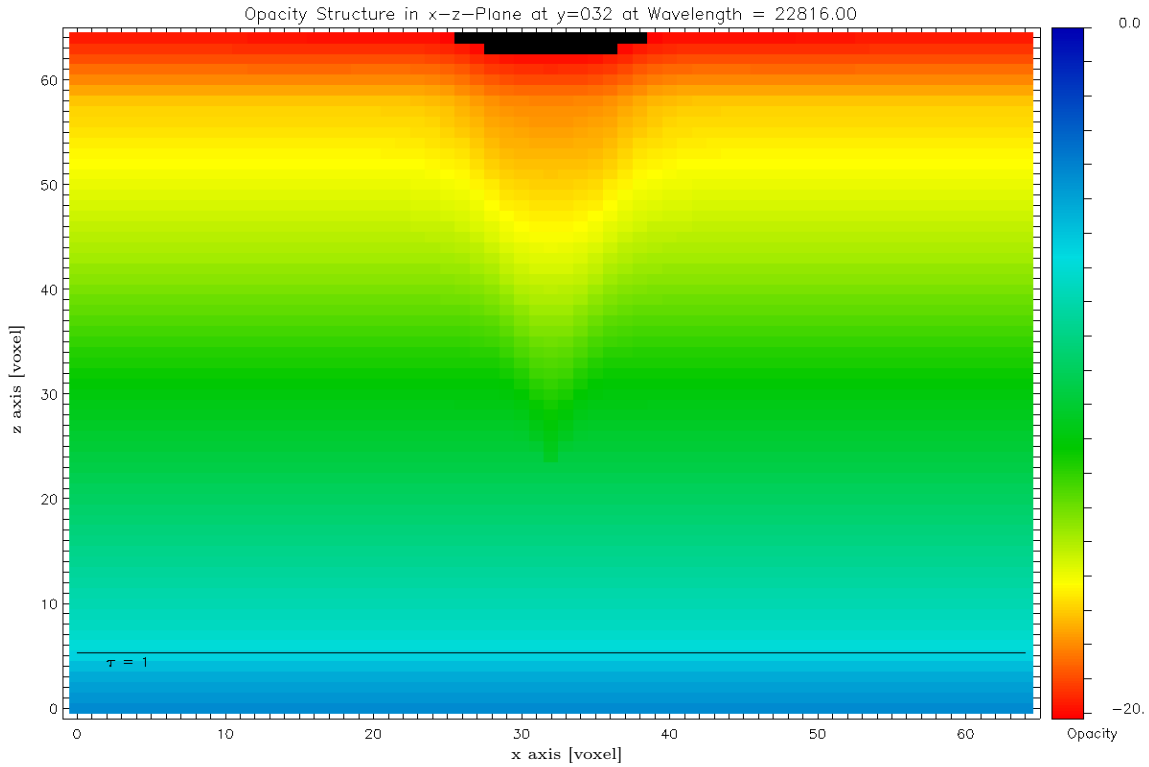

Figure 5.22: Opacity structure in x-z plane, calculated from the shallow conical model in a solar type atmosphere. The opacity is shown at a line wavelength point for an Mg I line at $\lambda = 22816$ Å, which is not affected by the sunspot. The opacity χ is color coded logarithmically from $10^{-20}\mathrm{cm}^{-1}$ to $10^{0}\mathrm{cm}^{-1}$. The black line marks the $\tau = 1$ level for a characteristic with $(\vartheta, \phi) = (0, 0)$.

to the quiet sun but drops in absolute intensity much in the same way that the quiet surface intensity does. A characteristic with an angle of $\mu \leq 0.2$ would correspond to an observation close to the rim of the stellar disk, where the line of sight runs almost parallel to the surface. This would not be a problem in a spherical star model, but in this case we used a grid with lateral periodic boundary conditions, which represents a semi infinite slab. The same sunspot is repeated over and over, so that even if not a single characteristic traverses the entire spot, every single characteristic passes through the top region of the spot multiple times. Since the top of the spot is one of the two zones of strongest increase in opacity at line wavelength, the darkening is stronger once more, than at steeper characteristics which traverse the top region only once. We can see the result of this effect, if we look at the visualisations in figure 5.23, where the spot gets smothed out first and is later smeared out so much that it spreads over the entire grid. If we look at characteristics even closer to the rim of the stellar disk with $\mu \longrightarrow 0$ ($\vartheta \longrightarrow 90°$), this effect would increase, since the number times the characteristic passes through the spot would go to infinity.

The brightening of sunspots is one of the effects that depend on the 3D shape of the spot, as can be seen by comparison of the two different models. A change to the shape of the spot changes the regions, in which the opacities change. Since limb variations allow us

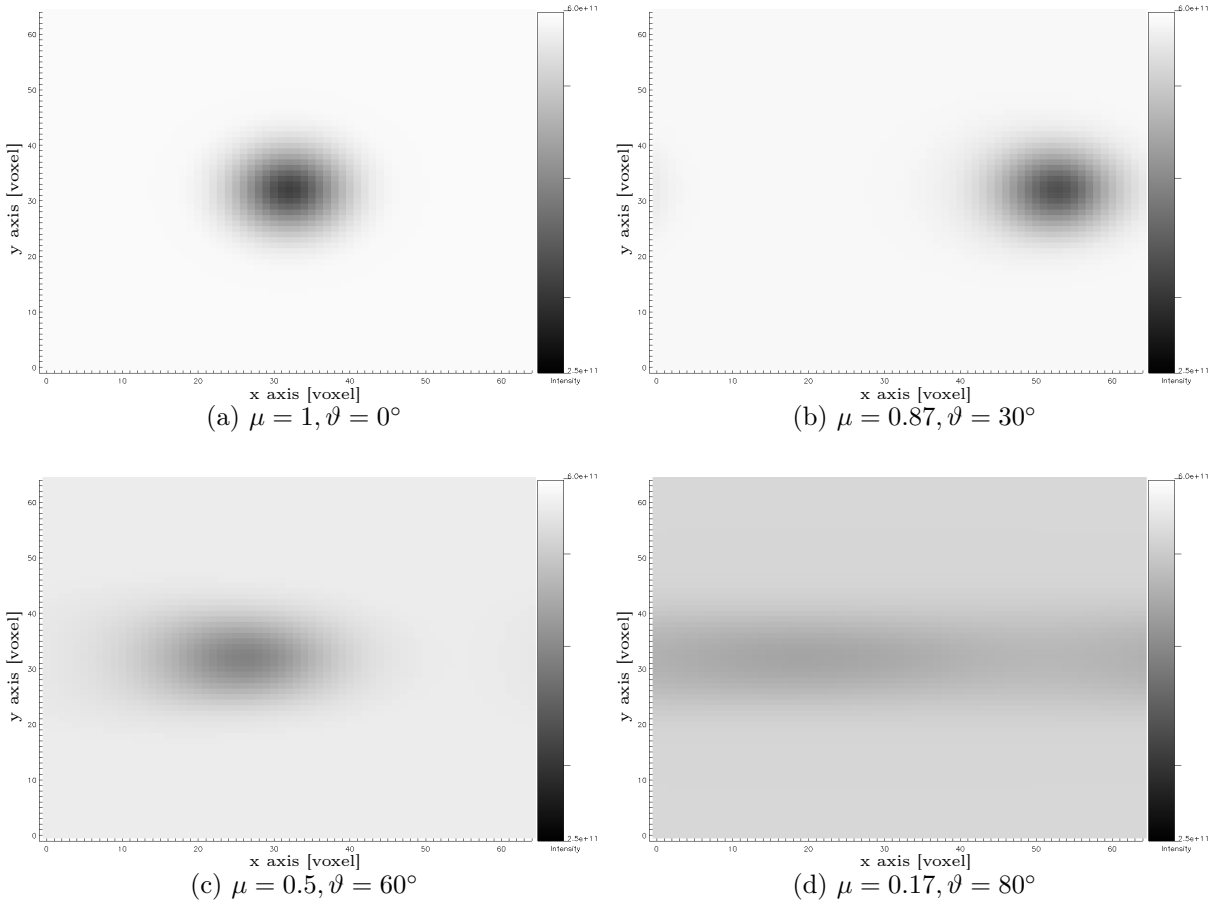

(a) $\mu = 1, \vartheta = 0°$ (b) $\mu = 0.87, \vartheta = 30°$

(c) $\mu = 0.5, \vartheta = 60°$ (d) $\mu = 0.17, \vartheta = 80°$

Figure 5.23: Intensity $I_\lambda(\lambda = \lambda_{\text{line}})$ at the surface of the grid seen under different angles of view $\mu = \cos(\vartheta)$ and $\phi = 0$. Intensity is color coded logarithmically between $2.5 \cdot 10^{11}\text{erg/cm}^2\text{/cm/sr}$ (black) and $6 \cdot 10^{11}\text{erg/cm}^2\text{/cm/sr}$ (white).

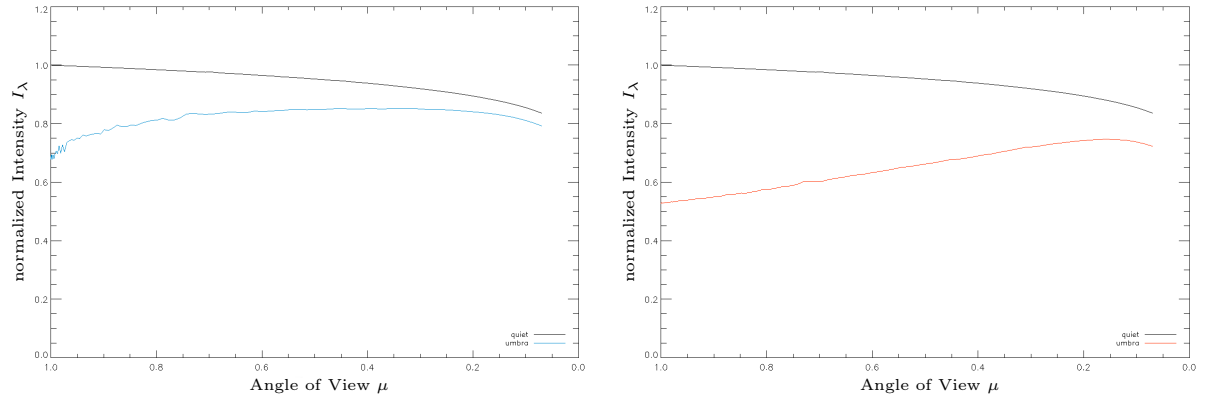

(a) shallow model (b) deep model

Figure 5.24: Center to limb variation for two different sunspot models, shown is intensity $I_\lambda(\lambda = \lambda_{\text{line}})$ for different characteristics μ, normalized to quiet $I_\lambda(\vartheta = 0)$ and direct view of $(\vartheta, \phi) = (0, 0)$. Black: Limb darkening in quiet continuum. Red: Umbra of deep conical sunspot. Blue: Umbra of shallow conical sunspot. Both calculations show signs of numerical noise due to spatial resolution of the voxel grid.

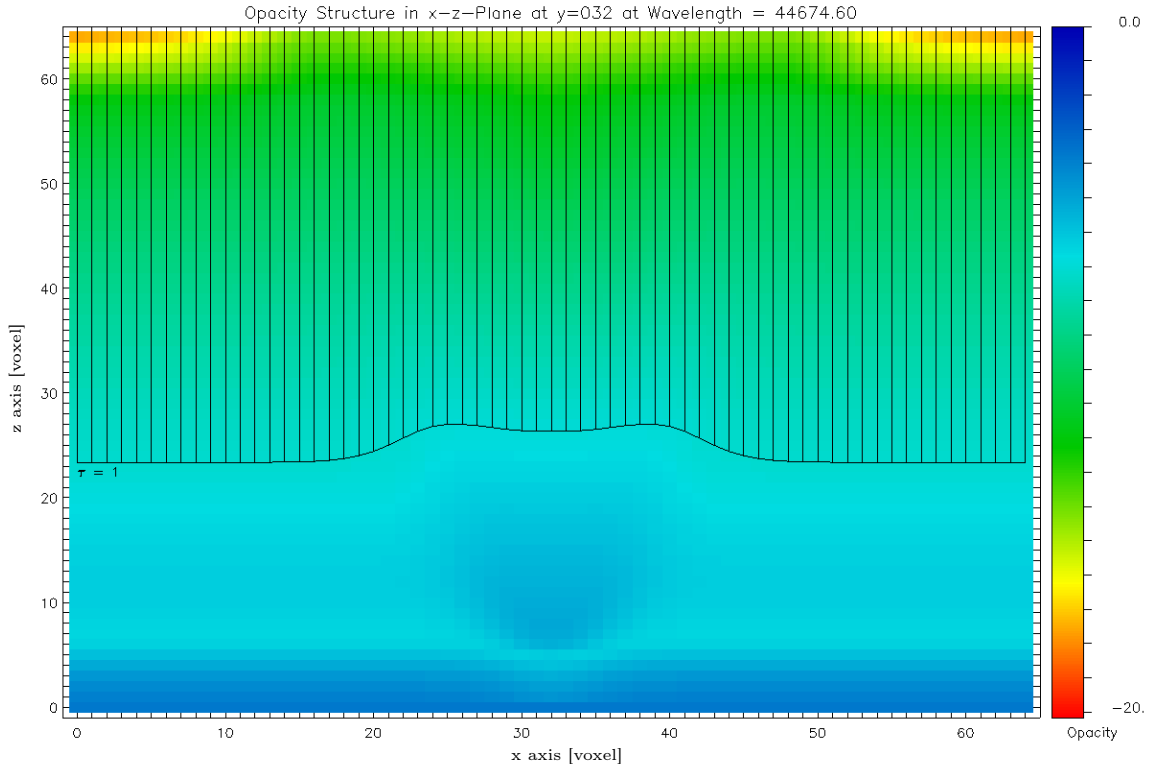

Figure 5.25: Opacity structure of the spot with characteristics and depth level of $\tau = 1$ for $(\vartheta, \phi) = (0, 0)$. The opacity χ is color coded from $10^{-20}\mathrm{cm}^{-1}$ to $10^{0}\mathrm{cm}^{-1}$.

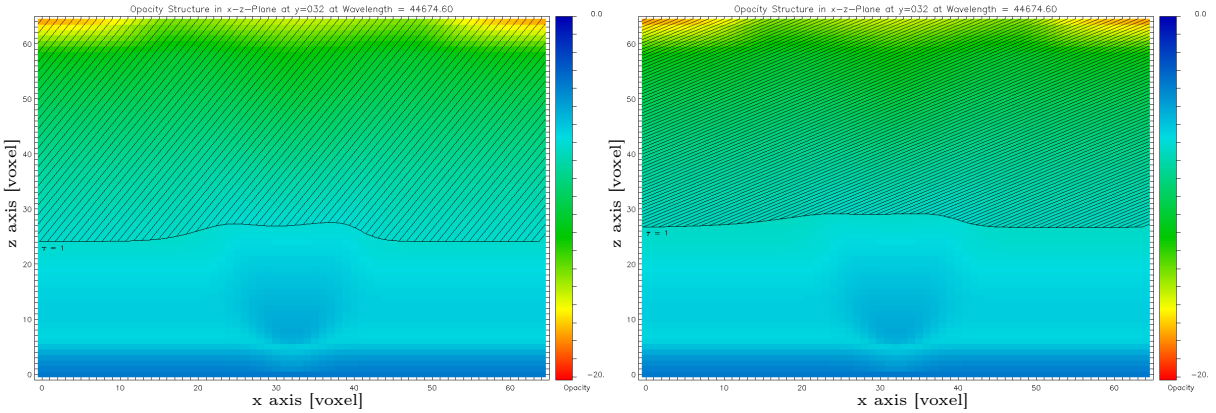

(a) $\mu = 0.87, \vartheta = 30°$ (b) $\mu = 0.5, \vartheta = 60°$

Figure 5.26: Opacity of a vertical slab of the grid through the center of the spot $\lambda = \lambda_{\mathrm{line}}$. Dark lines mark characteristics and depth of $\tau = 1$ for each characteristic of the grid and $\phi = 0$. The opacity χ is color coded from $10^{-20}\mathrm{cm}^{-1}$ to $10^{0}\mathrm{cm}^{-1}$.

to see different depth of the atmosphere, the shape of the $\tau = 1$ boundary that the spot produces is very important (e.g., figure 5.18). As shown in figure 5.24, even two models with the same basic shape but different depth and sizes can produce different behaviours.

Up to this point, we have calculated the center to limb variation of the intensity of an affected line at its center wavelength λ_{line}. We have shown that the continuum is affected less in the deep model and not at all in the shallow model. The opacity structure of the spot is quite different at continuum wavelength as well, as presented in figure 5.27. Thus, it is not surprising that we find a very different behaviour in figure 5.28. While the shallow model, where the intensity is not affected at all, does show the same limb darkening, as the quiet surface, the continuum of the deep model shows a moderate limb darkening, but then again a brightening, if we go to large angles ϑ. As before, this is an effect of the periodic boundary conditions, where, in this case, the optical thin regions of the spot are crossed multiple times, so that we see deeper into the atmosphere than without the spot.

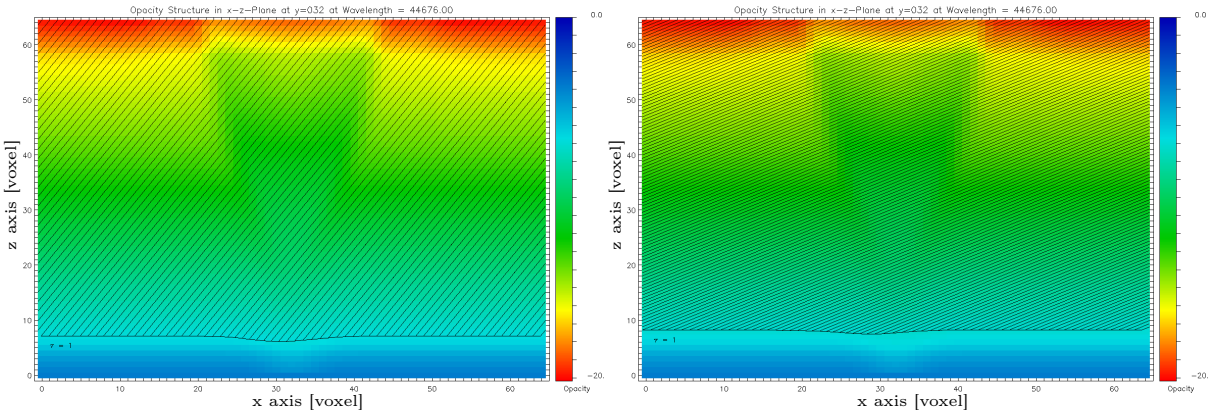

(a) $\mu = 0.87, \vartheta = 30°$ (b) $\mu = 0.5, \vartheta = 60°$

Figure 5.27: Opacity of a vertical slab of the grid through the center of the spot for $\lambda = \lambda_{\text{cont}}$. Dark lines mark characteristics and depth of $\tau = 1$ for each characteristic of the grid and $\phi = 0$. The opacity χ is color coded from 10^{-20}cm^{-1} to 10^{0}cm^{-1}.

5.4 NLTE total redistribution Scattering

In the previous sections, we have shown how the temperature difference of our sunspot models affects the star's surface intensity and how scattering enlarges the starspot in an NLTE test case, in which the temperature is changed, but the opacity is constant. Furthermore, we have calculated, how the change in temperature influences the opacity structure within the boundaries of the star. In this section we will combine both calculations. To achieve this, we use both the shallow and the deep model from the full PHOENIX/3D calculations and implement the temperature structure, and the opacities for both line and continuum into the input data for our two level solver. This was done by reading the continuum opacity from a point outside the CO line at $\lambda = 44674.6$ Å into χ_{cont} and use it to calculate the line opacity χ_{line} for the line center. The opacities in

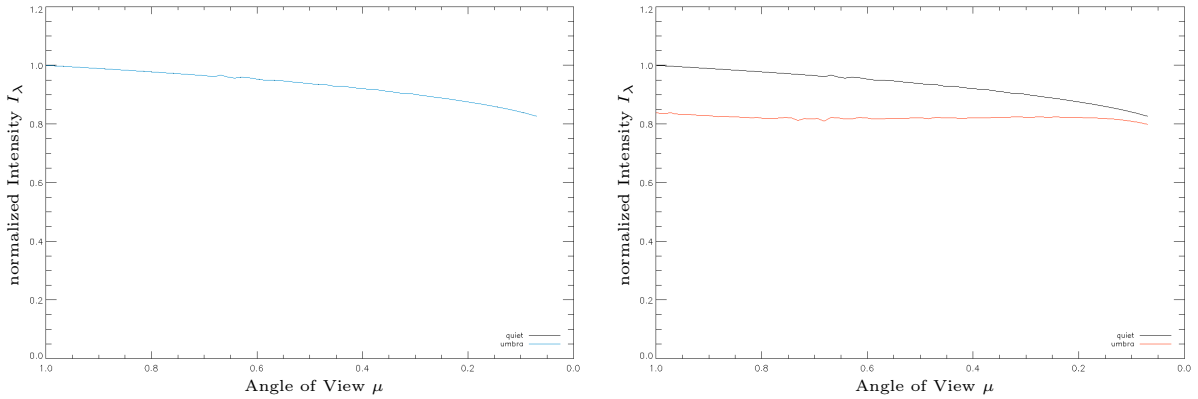

(a) shallow model (b) deep model

Figure 5.28: Center to limb variation for two different sunspot models, shown is intensity $I_\lambda(\lambda = \lambda_{\text{cont}})$ for different characteristics μ, normalized to quiet continuum and direct view of $(\vartheta, \phi) = (0, 0)$. Black: Limb darkening in quiet continuum. Red: Umbra of deep conical sunspot. Blue: Umbra of shallow conical sunspot.

between are then interpolated by use of a standard Gaussian line profile with a line width of $\Delta\lambda = 0.45$ Å.

With this set-up, we have solved the problem of radiative transfer for an LTE thermal emission and complete redistribution scattering. Once more, we used a grid of $n_x = n_y = n_z = 32$ and therefore 274 625 voxels. Due to the different presets of both solvers, the size of each voxel is here 15.38 km which leads to a total grid size of 1000 km, so that the spot is actually smaller.

Deep Model

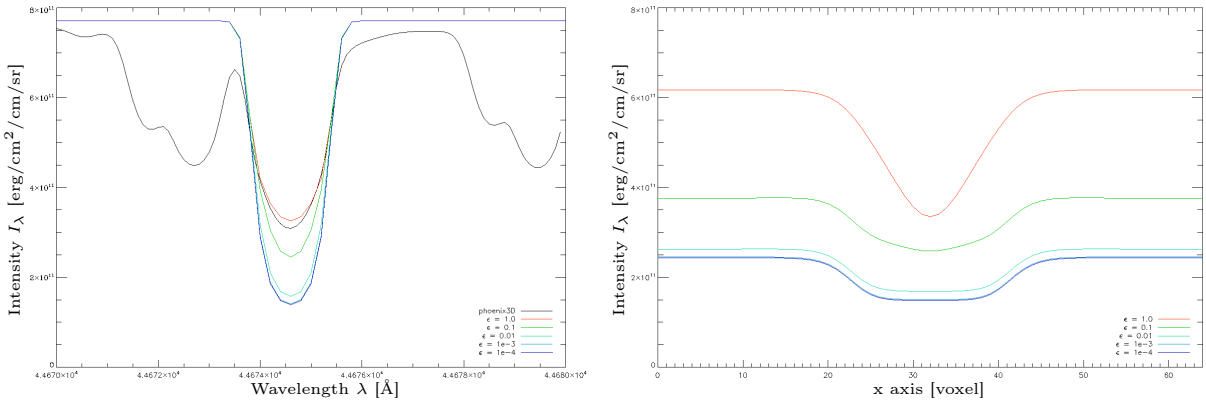

(a) intensity spectrum (b) lateral profile

Figure 5.29: Comparison of intensity for deep model and different scattering coefficients $\varepsilon_{\text{line}} = 1.0, 0.1, 10^{-2}, 10^{-3}$, and 10^{-4} both in spectrum at umbral center and lateral profile for $\lambda = \lambda_{\text{line}}$. Original spectrum from PHOENIX/3D Calculation is shown in black for comparison.

The results of this calculations for the deep models are presented in figure 5.29, which shows both the spectra of the two level calculations for different scattering coefficients $\varepsilon_{\text{line}}$, and the lateral profile at line center wavelength. We observe the same effect, as we were led to expect from the first calculations with the simple set-up in section 5.1. However, with the real temperature and opacity structure, the effect is more pronounced. The quiet surface and the penumbra are darker then before, while the umbra itself is likewise darker as before. Moreover, the contrast between umbra, penumbra and quiet surface has been diminished. What is even more interesting is that here scattering causes a much more pronounced change to the lateral intensity profile of the spot, than in the simple calculations with plane parallel opacity. The umbra widens and now forms a large center of the spot, where the intensity is spatially constant. This large umbral core is surrounded by the penumbra that is larger than before, but has not grown as much as the umbra. The formation of this umbral core proceeds with increasing influence of scattering.

The models with $\varepsilon_{\text{line}} = 10^{-2}$,$10^{-3}$, and 10^{-4} show that the constant umbra seems to be fully formed by $\varepsilon_{\text{line}} = 10^{-2}$, while any further increase affects the structure in total without doing much to the shape of the lateral profile. Consequently, the difference between the two models with the smallest epsilon is barely visible. At $\varepsilon_{\text{line}} = 10^{-1}$ we can see into a transition state between the fully formed constant umbral core and the lateral profile that is produced by the non scattering case. In our calculations, the effect is possibly limited by the fact that we included only line scattering.

This result is closer to the pictures of a very distinct sunspot umbra with little change to the intensity inside it that can be observed on the solar surface. This is evident, if we compare the visualisations in figure 5.30 to the real image in figure 4.1.

Shallow model

The same kind of simulation was done for a the shallow model configuration, to see if the effects are the same for an even smaller and less deep spot structure. The resulting umbral spectrum and lateral profile of the shallow spot model are shown in figure 5.31. The consequence of the introduction of total redistributive scattering is similar to the results we have presented for the deep model. Without scattering, the spot has a sharp profile with a very distinct minimum of intensity. If we increase the scattering coefficient $\varepsilon_{\text{line}}$, the overall contrast between spot and quiet surface is reduced, and the lateral profile changes. Note that we do not see an almost constant core of the umbra, as we have in the larger spot of the deep model. Nevertheless, the spot profile is smoothed out, as radiation is scattered into the spot. Even if the umbra does not show a constant darkening, the gradient of the profile is considerably smaller and spreads farther out. Even though the resulting lateral profile is different, the transformation is once again complete by $\varepsilon_{\text{line}} = 10^{-2}$ and the difference between $\varepsilon_{\text{line}} = 10^{-3}$ and $\varepsilon_{\text{line}} = 10^{-4}$ is negligible.

The effects of scattering that we already saw in the simple calculations in section 5.1, are definitely present again. The results of both calculations show that scattering reduces the overall darkening of the spot area. In this way, we can assume that in order to achieve the darkening of the spot, as expected from observations of the solar surface, we have to cool down our spot further, especially in the mid layers of our model. Since even the deep model is small for a sunspot, this is not too surprising.

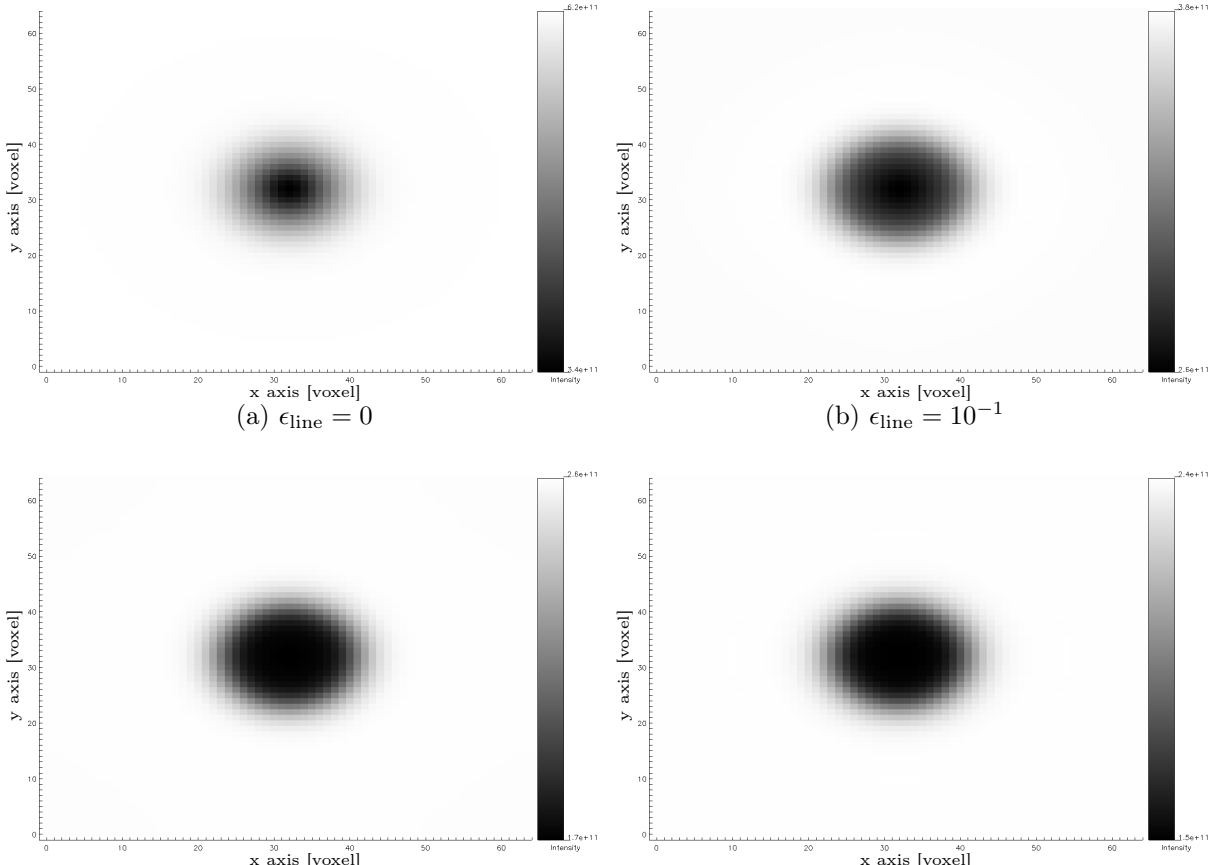

(a) $\epsilon_{\text{line}} = 0$ (b) $\epsilon_{\text{line}} = 10^{-1}$

(c) $\epsilon_{\text{line}} = 10^{-2}$ (d) $\epsilon_{\text{line}} = 10^{-4}$

Figure 5.30: Surface Intensity I_λ for $\lambda = \lambda_{\text{line}}$, as seen from directly above the grid with $(\vartheta, \phi) = (0, 0)$. Intensity is color coded logarithmically, scaled to the maximum and minimum intensity seen in each plot.

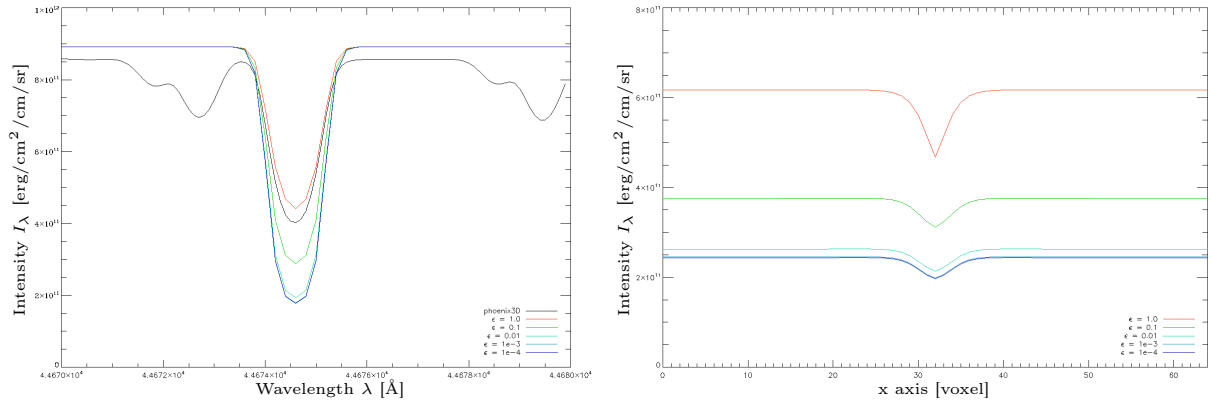

(a) intensity spectrum (b) lateral profile

Figure 5.31: Comparison of intensity for shallow model and different scattering coefficients $\varepsilon_{\text{line}} = 1.0, 0.1, 10^{-2}, 10^{-3}$, and 10^{-4} both in spectrum at umbral center and lateral profile for $\lambda = \lambda_{\text{line}}$. Original spectrum from PHOENIX/3D Calculation is shown in black for comparison.

5.5 Observable Spectra

We have compared the spectra of surface voxels of the umbra with the spectra of the quiet sun outside the spot. This has helped us to build a model that creates a distinct structure of umbra and penumbra on the surface of our grid structure. Yet, it remains impossible to resolve the surface of any star but the sun and, therefore, the surface intensity as well. For this reason, we have calculated the observable flux of our grid structure by summation over the z component of all surface voxels.

However, this only gives us the result for a small fraction out of the surface of a star. Of course, we could try to implement a sunspot like structure into the surface of a three dimensional grid that represents an entire star. Yet, the spatial resolution would have to be high enough to still resolve the spot with enough features, otherwise a too low resolution would hide any effects. Furthermore, a single spot on a stellar surface is unlikely to have any observable contribution to the total spectra. Conclusively, we would have to set up a model for a complete three dimensional surface of the star with a relevant coverage by a number of fully resolved spots. The computational demands for this would be high and most of the parameters we would have to put into the model would later be hidden by the integration over the surface.

With the current set-up, it is far more convenient to simply weight different surface voxels differently and therefore virtually add additional quiet surface voxels without increasing the computational demands. In this way, we can produce spectra for different levels of spot coverage of a star.

Figure 5.32 shows the result in form of integrated flux spectra for the different levels of coverage. Note that the total size of the surface, and thus the total flux is different for all three calculations, since we had to add different amounts of additional quiet voxels to achieve the different levels of spot coverage. The shown spectra were calculated with a resolution of 0.2 Å for a small wavelength band, where there are three absorption lines, from which two overlap each other, so that we see an even stronger effect, due to the addition of two overlapping affected line opacities.

Due to the fact that a star is usually only partly covered with sunspots, the effect on the integrated flux spectra is small. This might in part for the reason that our spot models are not as strongly darkened, as we would expect from observations of spots on the solar surface. With our current models, even if we assume a coverage of the stellar surface of more than one third, the variation to the strongest affected spectral line is less than one percent.

5.6 Resolution Tests

So far, every calculation was done with grids of either 226 981 or 274 625 voxels, so that the spatial resolution was limited to the about 20 km size of each voxel, as far as the physical set-up is concerned. In the earlier models, we have shown that discontinuities in temperature can have a huge influence on the results, even though the discontinuities that result from the finite size of the discretization of our physical parameters are small compared to those that resulted from the pre-sets of the early models, it would be interesting, in which way an increased spatial resolution has an influence on the results.

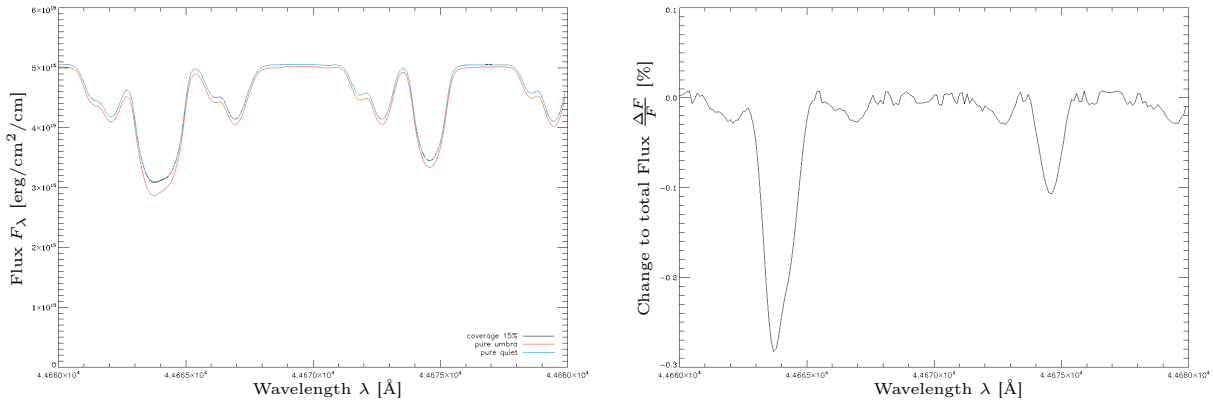

(a) 15 % coverage

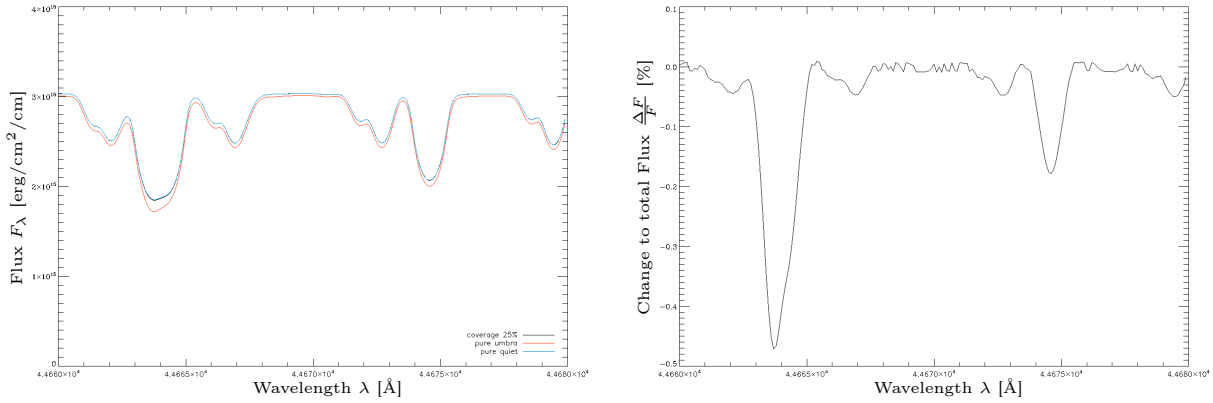

(b) 25 % coverage

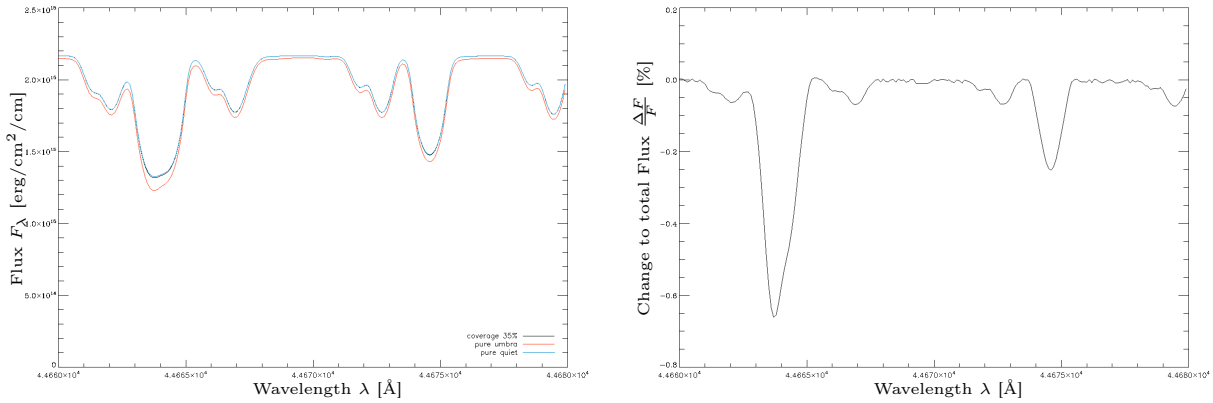

(c) 35 % coverage

Figure 5.32: Integrated spectra for different levels of spot coverage, calculated for the deep model. Left panels show total flux F_λ for covered surface, quiet surface (blue) and umbral spectrum (red). Right panels show flux difference $\frac{\Delta F_\lambda}{F_\lambda^{\text{quiet}}}$ in percent.

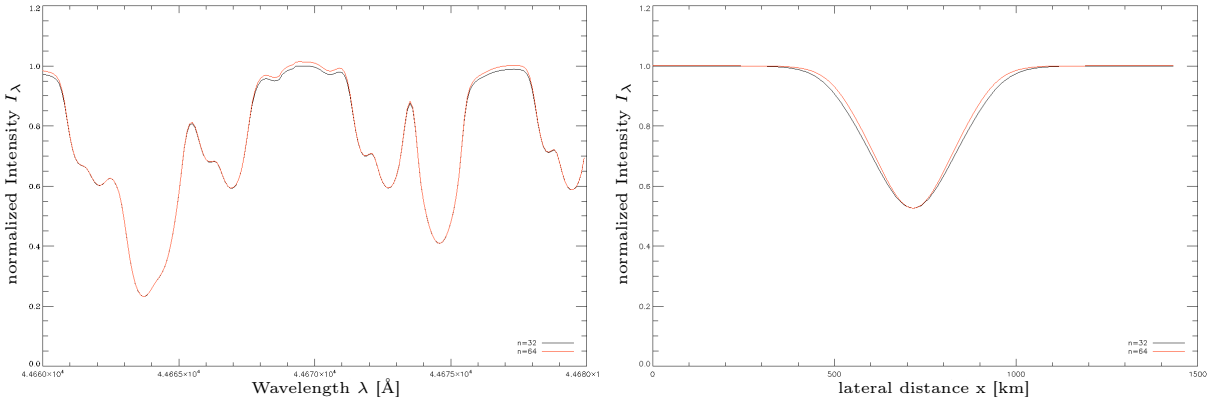

(a) Umbral spectrum (b) Lateral profile

Figure 5.33: Comparison between calculation with n = 64 (red) and n = 32 (black). Left panel: Spectrum of the center point of the umbra, normalized to maximum intensity of low resolution model. Right panel: Lateral intensity profile through the spot at $\lambda = \lambda_{\text{line}}$.

For comparison, we have calculated the *deep model* as described in table 5.1 for a grid of higher resolution with $n_x = n_y = n_z = 64$, which is equivalent to a total of 2 146 689 voxels. Each voxel then represents an element of volume with an edge length of $a_{\text{voxel}} = 11.19$ km, so that the total size of the grid is still about 1455 km.

Figure 5.33 shows a spectrum of the spots center surface voxel and a lateral profile through the spot at a line wavelength. In the umbral spectrum, we can see that the continuum points are brighter in the high resolution model, which means that the spot is less dark than before - here the lines are not affected but show the same reduced intensity. If we look at a line wavelength point's lateral profile through the spot, we can see that while the intensity at the center of the umbra is indeed unaffected, the intensity in the outer regions of the umbra and the penumbra has increased slightly, which is equivalent to a shrinking of the spot, which will appear smaller in this calculation than before.

If we just compare the temperature or opacity structures of different resolutions, we do not see any significant change that would be sufficient to explain these differences and why not the entire structure but different parts in different wavelength are affected. To solve this, we look at the temperature structure of a vertical cut through the grid and once again mark the levels of optical depth $\tau_\nu = 1.0$, which are relevant for the outgoing radiation and, as we have shown above, quite different for line and continuum. As shown in figure 5.34, the continuum at the umbra is dominated by a region with a high temperature gradient, thus the increased resolution has a stronger effect here, than in parts of the grid, where the temperature changes are smaller, because the difference between neighbouring voxels is smaller due to the increased spatial resolution.

The same is true for the changes to the lateral profile of the line wavelength. In the center of the spot, the temperature gradient is relatively small, while the rim of the umbra and the penumbra are generated by the transition regions, where the temperature gradient is higher, so that the increased resolution has a stronger influence. Basically, a voxel that has one temperature in the low resolution grid, is now represented by 8 voxels with different temperatures, even if the change over the entire length of two neighbouring voxels is the same.

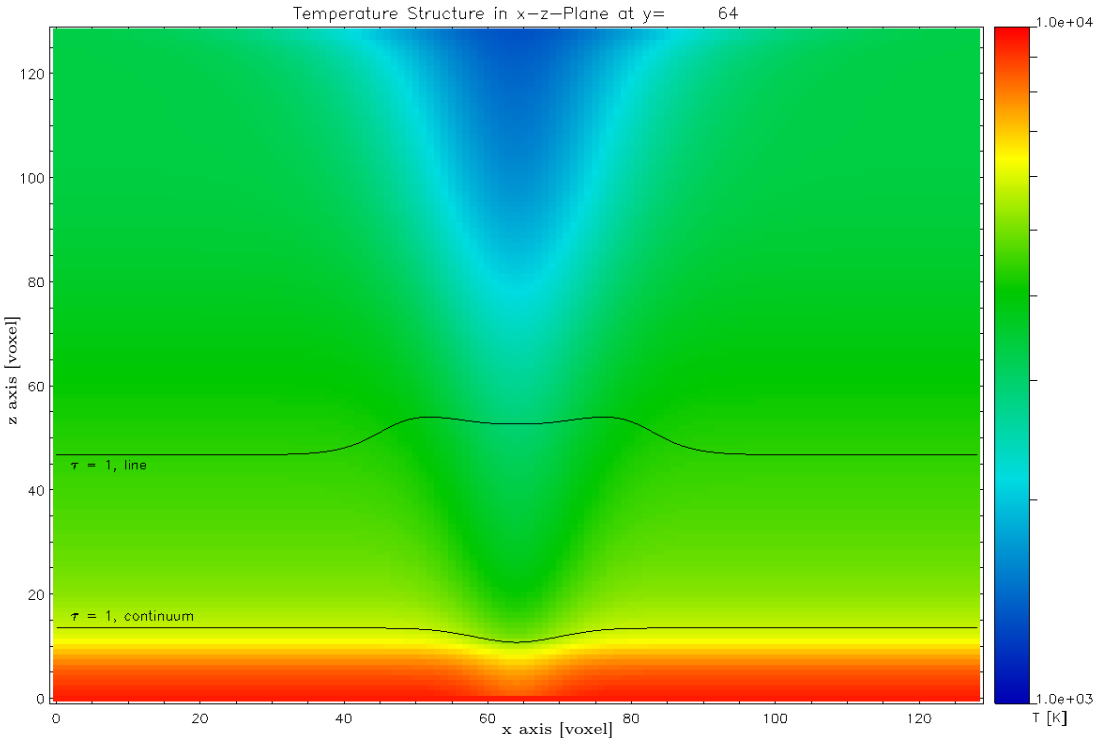

Figure 5.34: Temperature structure of the high resolution deep model with n = 64. Temperature is shown color coded logarithmically from 1000K to 10000K. The black lines mark the optical depth $\tau = 1$ for $\lambda = \lambda_{\text{line}}$ and $\lambda = \lambda_{\text{cont}}$ along characteristics with $(\vartheta, \phi) = (0, 0)$.

If we measure the mean distance between the lateral profiles for both resolutions, we find that the change in penumbral radius is of the order of

$$\Delta r_{\text{p}} \approx 11.8\text{km}$$

which is of the same order, as the increase in spatial resolution, and thus not very surprising. Of course it would be possible to further increase the spatial resolution, but at least as long as we use simple models, the gain does not seem to justify the increase in computational demand and storage requirements.

The spatial resolution is only one factor that can affect our calculations. The mean intensity J is calculated by Monte-Carlo integration with a uniform distribution of $n_\vartheta \cdot n_\phi$ characteristics. As we have mentioned previously in section 3.1, it is necessary to cover the full solid angle sufficiently. Otherwise the integral cannot be replaced by the Monte Carlo sum. In all previously discussed models, we used $n_\varphi = n_\vartheta = 64$ and therefore a total of 4096 evenly distributed characteristics. We have already tested the effect of spatial resolution on our calculations. It remains to study, if the number of characteristics we used is sufficient for the Monte Carlo integration.

For this test, we did another calculation with the deep model, using $n_\varphi = n_\vartheta = 128$, which represents a total of 16,384 characteristics. The results of this calculation both for the spectrum and the lateral profile can be seen in figure 5.35. The increase of the number

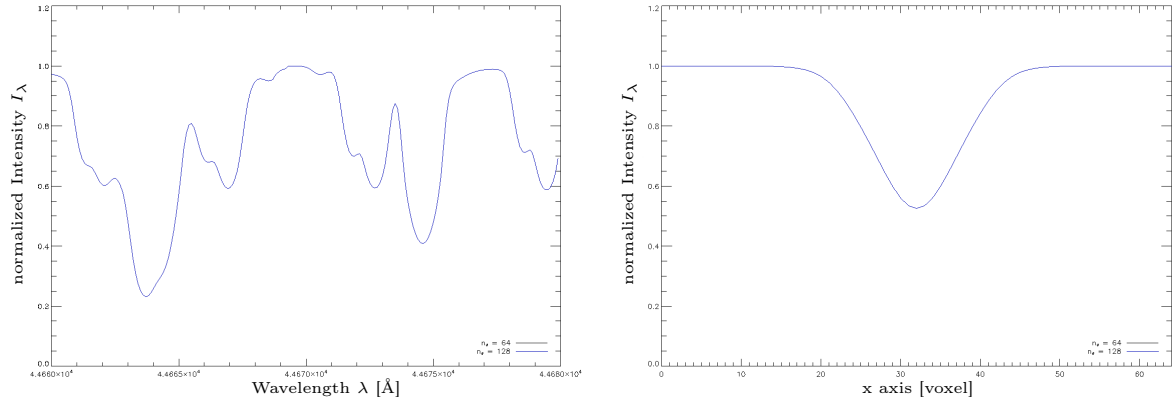

(a) Umbral spectrum (b) Lateral profile

Figure 5.35: Comparison between calculation with $n_\varphi = n_\vartheta = 128$ (blue) and $n_\varphi = n_\vartheta = 64$ (black). Left panel: Spectrum of the center point of the umbra, normalized to maximum intensity of low resolution model. Right panel: Lateral intensity profile through the spot at $\lambda = \lambda_{\text{line}}$.

of solid angles has caused no significant change to the spectrum or the lateral profile. The maximal difference in the umbral spectrum is of the order of

$$\max\left(\frac{\Delta I}{I}\right) \approx 10^{-7}$$

so a use of $n_\varphi = n_\vartheta = 64$ seems to be sufficiently reliable for our current models.

Chapter 6

Summary and Outlook

Over the course of this work, we successfully set up a number of different models to simulate the effects that the presence of a sunspot has on the stellar atmosphere and the stellar spectrum. We have shown that a region of reduced temperature in the solar atmosphere causes a similar region of reduced intensity on the solar surface, above the anomaly. The morphology of the dark spot on the surface depends on the shape of the anomaly underneath.

Further, we have investigated in which way the region of reduced temperature allows for the existence of molecules, in this case, carbon monoxide. As we expected, the carbon monoxide concentration inside the sunspot model is significantly increased by up to 20000 times, compared to the quiet solar atmosphere, with the highest increase beeing located at the surface of the star and at the bottom of our spot model. Again, the shape of the three dimensional anomaly that creates the spot is important for the distribution of CO molecules.

The overabundance of CO causes an increase in opacity inside the spot so that the opacity structure of the model varies strongly between continuum or not affected line wavelength points and those wavelength points of an affected molecular line such as carbon monoxide. This results in a much stronger darkening of the surface at affected wavelengths and, therefore, a deepening the lines. Even shallow models show an increase in line depth while the continuum remains unaffected. Models that affect the atmosphere up to deeper levels still show a more pronounce darkening at affected line wavelengths, than at unaffected points.

Furthermore, we have seen how complete redistribution line scattering has a strong influence on the lateral profile of a spot, especially in the penumbra, which is drawn farther outwards. With high scattering coefficients, we see a large umbra that is of more constant intensity than without scattering. The total area of the visible spot grows as well, leading to the conclusion that NLTE scattering enlarges the visible spot compared to the physical spot. This suggests that scattering is one of the reasons, if not the reason, while the umbra is of fairly constant brightness, even if the underlying temperature structure varies.

If we look at a resolved surface image of the sunspot, we can see that the three dimensional opacity structure of the spot model changes how the resulting spot is perceived under different angles of view. Our spot model would appear considerably brighter if seen close to the edge of the star, as opposed to the quiet surface effect of limb darkening. This is, of course, no true brightening of the spot itself, but solely depending on the an-

gle of view. Nevertheless, sunspots imaged under different angles of view would, in this way, represent a possibility to obtain information about the depth structure of the spot directly. However, it would be necessary to depart from the plane parallel and lateral periodic grid to correctly simulate spots at high angles of view.

From our models, we produced surface integrated spectra for the total Flux F_λ, since the surface of a distant star cannot be resolved directly with the currently available telescopes. Even though our models produce sunspot configurations that are relatively bright compared to observed solar sunspots, which is likely to be an indicator that even the deeper models are still too small, we can see that spot coverage affects the total spectra of a star. We have calculated different levels of spot coverage up to 35 % of the stars surface. The strongest effect to a line was of the order of 0.6% of the quiet total flux at the line center wavelength point.

In this work, we have shown that three dimensional spot structures in stellar atmospheres have a significant influence on the emerging spectrum. Of course, it is not possible to produce synthetic spectra for comparison for every possible configuration of starspots, due to the fact that the number of free parameters would be far too great. However, even the possibility to simulate different levels of coverage for a stellar surface would be valuable.

So far, we have used a plane parallel set-up as base for our sunspot models and very simple model assumptions. To produce synthetic spectra for comparison with observed data, it would, first, be necessary to improve the model we have. While our simple temperature structures prooved valuable for testing purposes, a more realistic temperature structure and spot size would be needed for a comparison with observational data. For this it would be possible to compare the model with data taken from sunspots, where we have the advantage of fully resolved surface structures.

Furthermore, it would be interesting to fully model sunspots in magnetohydrodynamics, which would provide a more realistic temperature structure and the possibility to include a realistic velocity field into the calculations. Since sunspots are generated by an magnetically induced anomaly in the stellar convection, we can expect that spectral lines that are produced in a spot are broadened differently than at the quiet surface. The inclusion of velocity fields into the radiative transfer simulations is possible either in the Eulerian or the Lagrangian frame, where both are already implemented in PHOENIX.

Bibliography

E. H. Avrett. Solutions of the Two-Level Line Transfer Problem with Complete Redistribution. *SAO Special Report*, 174:101–+, 1965.

T. Barman et al. in preperation.

E. Baron and P. H. Hauschildt. A 3D radiative transfer framework. II. Line transfer problems. *A&A*, 468:255–261, June 2007.

C. J. Cannon. Angular quadrature perturbations in radiative transfer theory. *Journal of Quantitative Spectroscopy and Radiative Transfer*, 13:627–633, 1973.

S. Catalano, K. Biazzo, A. Frasca, and E. Marilli. Measuring starspot temperature from line depth ratios. I. The method. *A&A*, 394:1009–1021, Nov. 2002.

S. Chitre. The Structure of sunspots. *Monthly Notices of the Royal Astronomical Society*, 126:431–+, 1963.

G. Galilei. *Istoria e Dimostrazioni intorno alle Macchie Solari*. Giacomo Mascardi, Rome, 1613.

H. Haken and H. C. Wolf. *Molekülphysik und Quantenchemie*. Springer, 5th edition, 2006.

P. H. Hauschildt. A fast operator perturbation method for the solution of the special relativistic equation of radiative transfer in spherical symmetry. *Journal of Quantitative Spectroscopy and Radiative Transfer*, 47:433–453, June 1992.

P. H. Hauschildt. Multi-level non-LTE radiative transfer in expanding shells. *Journal of Quantitative Spectroscopy and Radiative Transfer*, 50:301–318, Sept. 1993.

P. H. Hauschildt. Stellar/Planetary Atmospheres. Lecture notes, 2009.

P. H. Hauschildt and E. Baron. Numerical solution of the expanding stellar atmosphere problem. *Journal of Computational and Applied Mathematics*, 109:41–63, Sept. 1999.

P. H. Hauschildt and E. Baron. A 3D radiative transfer framework. I. Non-local operator splitting and continuum scattering problems. *A&A*, 451:273–284, May 2006.

P. H. Hauschildt and E. Baron. A 3D radiative transfer framework. III. Periodic boundary conditions. *A&A*, 490:873–877, Nov. 2008.

P. H. Hauschildt and E. Baron. A 3D radiative transfer framework. VI. PHOENIX/3D example applications. *A&A*, 509:A36+, Jan. 2010.

K. F. Huber. *Starspots and extra-solar planets in lightcurves and radial velocity measurements*. PhD thesis, Universität Hamburg, 2010.

G. Kron. The Probable Detecting of Surface Spots on AR Lacertae B. *Publications of the Astronomical Society of the Pacific*, 59:261, 1947.

D. Mihalas. *Stellar Atmospheres*. A Series of Books in Astronomy and Astrophysics. W. H. Freeman and Company, San Francisco, 1970.

D. Mihalas. *Stellar Atmospheres*. W. H. Freeman and Company, San Francisco, Second edition, 1978.

K.-C. Ng. Hypernetted chain solutions for the classical one-component plasma up to gamma equals 7000. *Journal of Chemical Physics*, 61:2680–2689, 1974.

G. L. Olson and P. B. Kunasz. Short characteristic solution of the non-LTE transfer problem by operator perturbation. I. The one-dimensional planar slab. *Journal of Quantitative Spectroscopy and Radiative Transfer*, 38:325–336, 1987.

R. J. Rutten. *Radiative Transfer in Stellar Atmospheres*. Utrecht University lecture notes, 8th edition, 2003.

A. Schweitzer. Modellatmosphären für M-Zwerge, Erweiterte Moleküllinienopazitäten und druckverbreiterte Linienprofile, 1995.

A. M. Seelmann. *3D radiative transfer in arbitrary velocity fields: The Eulerian approach*. PhD thesis, Universität Hamburg, 2011.

W. R. Smith and R. W. Missen. *Chemical Reaction Equilibrium Analysis: Theory and Algorithms*. John Wiley & Sons, 1982.

J. H. Thomas and N. O. Weiss. *Sunspots and Starspots*. Number 46 in Cambridge Astrophysics Series. Cambridge University Press, 2008.

H. Uitenbroek. The CO Fundamental Vibration-Rotation Lines in the Solar Spectrum. I. Imaging Spectroscopy and Multidimensional LTE Modeling. *The Astrophysical Journal*, 531:571–584, Mar. 2000a.

H. Uitenbroek. The CO Fundamental Vibration-Rotation Lines in the Solar Spectrum. II. Non-LTE Transfer Modeling in Static and Dynamic Atmospheres. *The Astrophysical Journal*, 536:481–493, June 2000b.

Acknowledgment

Zunächst möchte ich mich bei meinem Betreuer Peter Hauschildt und der PHOENIX Gruppe der Hamburger Sternwarte für die freundliche Aufnahme und die Betreuung während meiner Diplomarbeit bedanken. Insbesondere erwähnt sei hier die geduldige Beantwortung aller Fragen zu PHOENIX, Fortran, IDL, LaTeX und anderen Themen. Weiterhin danke ich meinen Bürokollegen Ernst Lexen, Sören Witte und Andreas Seelmann für die angenehme Arbeitsatmosphäre bei uns im Büro. Mein Dank gilt ebenfalls allen Korrekturlesern.
Die Rechnungen für diese Arbeit wurden zu etwa gleichen Teilen im Rechenzentrum des Norddeutschen Verbunds zur Förderung des Hoch- und Höchstleistungsrechnens (HLRN), sowie auf dem Cluster NATHAN der Hamburger Sternwarte durchgeführt. Hierbei möchte ich mich insbesondere bei Andreas Schweitzer bedanken, welcher NATHAN und alle anderen lokalen Cluster betreut und am Laufen hält.

Mein besonderer Dank gilt meinen besten Freunden Ricarda Laasch, sowie Andrea und Stephan Klumpp. Es ist nicht nur der Weg, der zählt, sondern die Menschen, mit denen man ihn gemeinsam beschreiten kann - und was das betrifft, könnte ich mir keine besseren Weggefährten wünschen.
An dieser Stelle möchte ich mich ebenfalls bei Herrn Doktor Waldemar Tausendfreund von der Arbeitsgruppe *Faszination Physik* bedanken, für die Möglichkeit, eben diese Faszination schon zu meiner Schulzeit zu vertiefen und immer wieder neu zu finden.
Danke natürlich auch an meine Eltern, für all die Möglichkeiten, die ich habe und dafür, dass ihr mich immer ermutigt habt, meinen Träumen nachzujagen.

Abschließend und mit einem Augenzwinkern, ein Dank an das Universum an sich, im Allgemeinen und im Besonderen - dafür, dass es ein faszinierender, rätselhafter Ort ist, der Phantasie beflügelt und zum Nachdenken anregt - und in dem es immer mindestens eine Sache gibt, die wir noch nicht erforscht haben. Es wäre ja ansonsten auch unheimlich langweilig.

Erklärung zur Diplomarbeit

Hiermit versichere ich, diese Diplomarbeit eigenhändig angefertigt zu haben. Hierbei habe ich ausschließlich die angegebenen Quellen und Hilfsmittel verwendet. Mit einer Veröffentlichung dieser Diplomarbeit durch die Universität Hamburg erkläre ich mich einverstanden.

(Alexander Berkner)
Hamburg, September 27, 2011